Research Square

Preprints are preliminary reports that have not undergone peer review.
They should not be considered conclusive, used to inform clinical practice,
or referenced by the media as validated information.

Nonlinear Uncertainty Transformation for Geometry-Aware Spacecraft Optical Navigation

Ridma Ganganath
Iowa State University
Simone Servadio
servadio@iastate.edu

Iowa State University

Research Article

Keywords: Spacecraft navigation, optical navigation, fully multiplicative, unscented Kalman filtering, sparse Gauss–Hermite quadrature, misalignment calibration

Posted Date: November 10th, 2026

DOI: https://doi.org/10.21203/rs.3.rs-11472028/v1

License: This work is licensed under a Creative Commons Attribution 4.0 International License.
Read Full License

Additional Declarations: No competing interests reported.

Nonlinear Uncertainty Transformation for Geometry-Aware Spacecraft Optical Navigation

Ridma Ganganath[1] and Simone Servadio[2*]

[1,2]Department of Aerospace Engineering, Iowa State University, Ames, 50011, Iowa, The USA.

*Corresponding author(s). E-mail(s): servadio@iastate.edu;
Contributing authors: ridma@iastate.edu;

Abstract

Autonomous optical navigation requires a spacecraft to determine where it is and how it is oriented using onboard measurements. Small optical-tracker mounting errors couple the attitude and orbit estimates and can bias both if not estimated. This work treats spacecraft attitude, orbit, and the three-axis alignment of two optical trackers as a single estimation problem using stellar and celestial-body direction measurements. The formulation preserves the multiplicative geometry of attitude and unit-vector measurements and extends the nonlinear uncertainty treatment from unscented sampling to sparse Gauss–Hermite quadrature (SGHQ) at Levels 2 and 3. A multiplicative extended Kalman filter (MEKF), a fully multiplicative unscented Kalman filter (FM-UKF), and fully multiplicative sparse Gauss–Hermite quadrature filters (FM-SGHQFs) at Levels 2 and 3 are evaluated under identical dynamics, measurements, calibration states, and noise realizations. Monte Carlo results show little separation at the fine estimator-cycle interval, but clear differences at the coarse estimator-cycle interval. The FM-UKF and Level 3 FM-SGHQF retain close agreement between predicted covariance and empirical Monte Carlo dispersion, whereas the implemented MEKF loses consistency and the Level 2 FM-SGHQF becomes overconfident. Among the methods considered, the FM-UKF provides the best balance between statistical consistency and computational cost across the investigated regimes.

Keywords: Spacecraft navigation, optical navigation, fully multiplicative, unscented Kalman filtering, sparse Gauss–Hermite quadrature, misalignment calibration

1 Introduction

Spacecraft operation without continuous ground-based radiometric tracking requires greater onboard navigation autonomy. Optical measurements provide one means of supporting this autonomy by using stars and solar-system bodies as inertial and navigation references [1]. Celestial-body observations have been studied for autonomous navigation, including beacon selection and onboard orbit determination [2–4], and have also been incorporated into experimental and flight optical-navigation architectures [5, 6]. Recent development supported by the National Aeronautics and Space Administration (NASA), including the Optical Deep-Space Instrument for Navigation (ODIN), similarly combines multiple optical channels with autonomous target determination, attitude estimation, and optical position estimation for small-spacecraft applications [7]. These developments motivate estimation architectures in which stellar and celestial-body observations are processed within a common navigation system. In such a formulation, attitude, translation, and sensor alignment become coupled through the optical measurement model.

Spacecraft alignment parameters have previously been estimated in flight rather than treated as perfectly known calibration constants [8–10]. Simultaneous camera calibration with orbit and attitude reconstruction has also been demonstrated using optical imagery, for example in the Hayabusa2 optical-camera analysis of Kikuchi et al[11]. That work addressed image distortion and viewing geometry through a batch image-based reconstruction. The problem considered here differs from these formulations by retaining two optical-tracker mounting rotations as three-axis states within a recursive attitude–orbit estimator. Stellar measurements from each tracker constrain attitude and tracker alignment, while ephemeris-referenced celestial-body directions additionally couple the translational state through target-relative geometry. Celestial aberration is also included in the measurement model, introducing a direct dependence on spacecraft velocity [5, 12–14].

This coupled formulation also combines state and measurement variables with different geometries. Spacecraft attitude is represented globally by a unit quaternion, while the rest of the states are represented in Euclidean space. Quaternion uncertainty is therefore expressed locally by a three-dimensional rotation error rather than by an additive four-dimensional quaternion error [15–19]. Local rotational-error representations remain common in multiplicative and Lie-group attitude filtering [20, 21], including sigma-point formulations in which local attitude perturbations are injected into the quaternion, propagated through the nonlinear dynamics, and recentered about a quaternion mean [22, 23]. The optical measurements introduce a corresponding geometric constraint: each normalized line-of-sight (LOS) direction lies on $\mathbb{S}^2$. Direction uncertainty is therefore represented through rotational perturbations and tangent-space residuals rather than ordinary Euclidean subtraction [24, 25].

Nonlinear dynamics and measurement models distort the propagated uncertainty, so that even a Gaussian prior does not remain Gaussian. The estimators considered here all retain a Gaussian approximation but differ in how accurately they compute its mean and covariance. The multiplicative extended Kalman filter (MEKF) is retained here as a first-order comparison baseline, propagating local covariance

through first-order state and measurement linearizations, whereas sigma-point methods approximate the transformed moments by evaluating the nonlinear mappings at deterministic points. The unscented transformation provides a widely used deterministic moment approximation [26–30] and has been adapted to multiplicative spacecraft attitude estimation [22, 25]. Coupled attitude–orbit estimation has also been considered using a reduced sigma-point unscented filter with magnetometer and Sun-sensor measurements [31]. That formulation treats the coupled roto-translational state, but not simultaneous optical-tracker mounting calibration with multiplicative unit-vector measurements. The uncertainty transformation used for this coupled optical-navigation problem therefore remains a separate consideration.

Beyond the unscented transformation, Gauss–Hermite quadrature provides a deterministic approximation of Gaussian-weighted moments with increasing polynomial exactness as the quadrature order is increased [32]. Its conventional multidimensional construction, however, uses tensor products of one-dimensional rules, causing the number of quadrature points to grow exponentially with dimension. Smolyak sparse-grid constructions reduce this growth by combining selected tensor-product rules [33–35]. Sparse Gauss–Hermite quadrature filtering was subsequently applied separately to spacecraft attitude and orbit estimation [36, 37], and the sparse-grid quadrature filter introduced an adjustable quadrature level [38]. Sparse quadrature was later applied to vision-based relative navigation with simultaneous estimation of relative orbit, relative attitude, and gyroscope bias [39], while adaptive formulations varied the quadrature level during estimation to balance integration accuracy and computational cost [40]. However, the coupled absolute attitude–orbit–calibration problem, with constraints coming from hardware implementation, has not been considered yet. This paper proposes a full attitude and orbit recovery with two three-axis optical-tracker misalignment estimations while maintaining multiplicative unit-vector measurements.

A preliminary study of the coupled fully multiplicative unscented Kalman filter (FM-UKF) formulation for this attitude–orbit–calibration problem was introduced in [41]. The present journal version retains the coupled 21-dimensional formulation and multiplicative direction-measurement geometry and extends the nonlinear uncertainty treatment to sparse Gauss–Hermite quadrature. The journal-specific contributions are: (i) fully multiplicative SGHQ filters at sparse-grid Levels 2 and 3 with augmented process and rotational measurement uncertainty; (ii) a controlled comparison of the MEKF, FM-UKF, and both FM-SGHQFs under the same dynamics, stochastic model, calibration states, and optical measurement geometry; and (iii) an evaluation of estimation accuracy, statistical consistency, and computational cost across fine- and coarse-step estimator cycles. The geometric effect of multiplicative and additive-normalized direction-noise mappings is also examined to motivate the multiplicative optical measurement model used by all four estimators.

The remainder of this paper is organized as follows. Section 2 defines the common state, dynamics, stochastic model, and optical measurement geometry. Section 3 examines the geometric effect of additive-normalized and multiplicative direction-measurement noise on $\mathbb{S}^2$. Sections 4 and 5 present the FM-UKF and FM-SGHQF formulations, followed by the MEKF comparison baseline. Section 7 presents the

Monte Carlo accuracy, statistical consistency, and computational-cost results. Finally, Section 8 summarizes the main findings.

2 Problem Formulation

The estimation problem evolves on a mixed geometric state space. The spacecraft attitude is represented by a unit quaternion on $\mathbb{S}^3$, optical line-of-sight measurements lie on $\mathbb{S}^2$, and the angular-rate, bias, orbital, and calibration states are Euclidean. The estimated state is

$$\boldsymbol{x} \triangleq (\boldsymbol{q}, \boldsymbol{\omega}, \boldsymbol{b}, \boldsymbol{r}, \boldsymbol{v}, \boldsymbol{\mu}_1, \boldsymbol{\mu}_2), \qquad \boldsymbol{q} \in \mathbb{S}^3, \quad \boldsymbol{\omega}, \boldsymbol{b}, \boldsymbol{r}, \boldsymbol{v}, \boldsymbol{\mu}_1, \boldsymbol{\mu}_2 \in \mathbb{R}^3, \tag{1}$$

where $\boldsymbol{q} = [\boldsymbol{q}_v^\top, q_4]^\top$ is the scalar-last body-to-inertial attitude quaternion, $\boldsymbol{\omega}$ is the body angular velocity, $\boldsymbol{b}$ is the gyroscope bias, $\boldsymbol{r}$ and $\boldsymbol{v}$ are the inertial position and velocity, and $\boldsymbol{\mu}_1, \boldsymbol{\mu}_2$ are the residual optical-tracker misalignment rotation-vector coordinates. Their rotational action is

$$T(\boldsymbol{\mu}_j) = \exp([\boldsymbol{\mu}_j]_\times) \in SO(3), \qquad j = 1, 2. \tag{2}$$

which represents the resulting rotation matrix given the misalignment vectors. Because the quaternion is constrained, uncertainty is represented in the 21-dimensional local error state

$$\boldsymbol{e} \triangleq \left[\delta\boldsymbol{\theta}^\top \ \delta\boldsymbol{\omega}^\top \ \delta\boldsymbol{b}^\top \ \delta\boldsymbol{r}^\top \ \delta\boldsymbol{v}^\top \ \delta\boldsymbol{\mu}_1^\top \ \delta\boldsymbol{\mu}_2^\top\right]^\top \in \mathbb{R}^{21}. \tag{3}$$

The local retraction is defined by right-multiplicative attitude injection and additive Euclidean injection:

$$\boldsymbol{x} = \hat{\boldsymbol{x}} \oplus \boldsymbol{e} \triangleq \left(\hat{\boldsymbol{q}} \otimes \mathrm{Exp}_q(\delta\boldsymbol{\theta}),\, \hat{\boldsymbol{\omega}} + \delta\boldsymbol{\omega},\, \hat{\boldsymbol{b}} + \delta\boldsymbol{b},\, \hat{\boldsymbol{r}} + \delta\boldsymbol{r},\, \hat{\boldsymbol{v}} + \delta\boldsymbol{v},\, \hat{\boldsymbol{\mu}}_1 + \delta\boldsymbol{\mu}_1,\, \hat{\boldsymbol{\mu}}_2 + \delta\boldsymbol{\mu}_2\right), \tag{4}$$

where

$$\mathrm{Exp}_q(\boldsymbol{\phi}) = \begin{bmatrix} \dfrac{\sin(\|\boldsymbol{\phi}\|/2)}{\|\boldsymbol{\phi}\|}\boldsymbol{\phi} \\ \cos(\|\boldsymbol{\phi}\|/2) \end{bmatrix}, \qquad \mathrm{Exp}_q(\boldsymbol{0}_3) = \begin{bmatrix} \boldsymbol{0}_3 \\ 1 \end{bmatrix}. \tag{5}$$

The inverse local attitude error is obtained from

$$\delta\boldsymbol{q} = \hat{\boldsymbol{q}}^* \otimes \boldsymbol{q}, \qquad \delta\boldsymbol{\theta} = \mathrm{Log}_q(\delta\boldsymbol{q}), \tag{6}$$

where $\otimes$ indicates the quaternion multiplication, Log_q is the inverse map of Exp_q, and with the representative of $\delta\boldsymbol{q}$ chosen to have nonnegative scalar part. The Euclidean components of $\boldsymbol{e} = \boldsymbol{x} \ominus \hat{\boldsymbol{x}}$ are obtained by ordinary subtraction. The nominal process model combines rigid-body attitude motion and two-body translational motion,

$$\dot{\boldsymbol{q}} = \frac{1}{2}\Omega(\boldsymbol{\omega})\boldsymbol{q}, \qquad \dot{\boldsymbol{\omega}} = J^{-1}\left(\boldsymbol{M}_c - \boldsymbol{\omega} \times J\boldsymbol{\omega}\right), \tag{7}$$

$$\dot{\boldsymbol{b}} = \boldsymbol{0}_3, \qquad \dot{\boldsymbol{\mu}}_1 = \boldsymbol{0}_3, \qquad \dot{\boldsymbol{\mu}}_2 = \boldsymbol{0}_3, \tag{8}$$

$$\dot{\boldsymbol{r}} = \boldsymbol{v}, \qquad \dot{\boldsymbol{v}} = -\mu_g \frac{\boldsymbol{r}}{\|\boldsymbol{r}\|^3}. \tag{9}$$

where J is the spacecraft inertia matrix, $\boldsymbol{M}_c$ is the applied body torque, and μ_g is the central-body gravitational parameter. For the scalar-last quaternion convention,

$$\Omega(\boldsymbol{\omega}) = \begin{bmatrix} 0 & \omega_z & -\omega_y & \omega_x \\ -\omega_z & 0 & \omega_x & \omega_y \\ \omega_y & -\omega_x & 0 & \omega_z \\ -\omega_x & -\omega_y & -\omega_z & 0 \end{bmatrix}. \tag{10}$$

The nominal gyroscope-bias and tracker-misalignment dynamics are zero, while their stochastic variations are modeled as continuous-time random walks. Angular and translational acceleration process uncertainty is also included. The continuous-time process-noise model is discretized over each estimator interval to obtain the 21-dimensional local process covariance $Q_{d,k-1}$. Therefore, the corresponding true biases and misalignment change in time according to a Brownian motion, mimicking thermal perturbations. The corresponding process-noise amplitudes are given in Table 1.

2.1 Gyroscope Measurement Model

The gyroscope provides a direct measurement of angular velocity corrupted by bias and white noise:

$$\boldsymbol{y}_{g,k} = \boldsymbol{\omega}_k + \boldsymbol{b}_k + \boldsymbol{\nu}_{g,k}, \qquad \boldsymbol{\nu}_{g,k} \sim \mathcal{N}\left(\boldsymbol{0}_3, R_g\right). \tag{11}$$

This measurement is processed as a Euclidean vector measurement. In contrast, the star-tracker and celestial-body line-of-sight measurements are processed as unit-vector measurements on $\mathbb{S}^2$.

2.2 Multiplicative Direction Measurement Model

The spacecraft carries two optical trackers with known nominal mounting rotations $T_{S_1B,0}$ and $T_{S_2B,0}$ and residual unknown three-axis misalignments $\boldsymbol{\mu}_1$ and $\boldsymbol{\mu}_2$. Measurements from a given tracker share the same mounting and residual misalignment. Figure 1 summarizes the coordinate frames and optical measurement geometry.

For a target a observed by tracker j, the noiseless predicted direction is

$$h_{j,a}(\boldsymbol{x}) = T(\boldsymbol{\mu}_j)\, T_{S_jB,0}\, T_{BI}(\boldsymbol{q})\, \boldsymbol{u}_{I,\mathrm{obs}}^{(a)} \in \mathbb{S}^2, \tag{12}$$

where $T_{S_jB,0}$ is the nominal body-to-tracker mounting rotation, $T(\boldsymbol{\mu}_j)$ is the residual misalignment rotation of Eq. (2), and $\boldsymbol{u}_{I,\mathrm{obs}}^{(a)}$ is the apparent inertial target direction. The optical measurement is modeled with multiplicative rotational noise [24, 25],

$$\boldsymbol{y}_{j,a} = T(\boldsymbol{\eta}_{j,a})\, h_{j,a}(\boldsymbol{x}), \qquad T(\boldsymbol{\eta}_{j,a}) = \exp([\boldsymbol{\eta}_{j,a}]_\times), \qquad \boldsymbol{\eta}_{j,a} \sim \mathcal{N}\left(\boldsymbol{0}_3, \sigma_{u,a}^2 I_3\right). \tag{13}$$

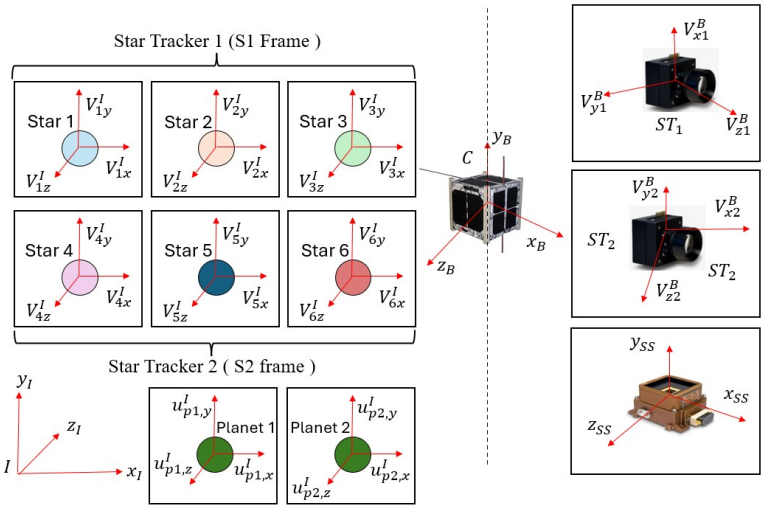


Fig. 1: Optical measurement geometry for the joint attitude–orbit–tracker-misalignment estimation problem.

Here $\sigma_{u,a}$ is the per-axis rotational measurement standard deviation. For an identified star, the inertial reference direction is obtained from the star catalogue. For a celestial body a, the geometric inertial line of sight is

$$\boldsymbol{u}_{I,\mathrm{true}}^{(a)} = \frac{\boldsymbol{p}_{I,a} - \boldsymbol{r}}{\|\boldsymbol{p}_{I,a} - \boldsymbol{r}\|}, \tag{14}$$

where $\boldsymbol{p}_{I,a}$ is the inertial position of the observed body. The apparent direction $\boldsymbol{u}_{I,\mathrm{obs}}^{(a)}$ is obtained from the aberration model of Section 2.3. Thus, celestial-body measurements depend on spacecraft position through Eq. (14), while aberration introduces the velocity dependence. Because rotation about the line of sight does not change the measured direction, each unit-vector observation contains two independent local measurement components.

2.3 Celestial Aberration

Celestial aberration is included because spacecraft velocity shifts the apparent optical direction from the geometric line of sight. Following Andreis et al. [4], let $\boldsymbol{u}_{I,\mathrm{obs}}^{(a)} \in \mathbb{S}^2$ denote the apparent inertial direction of target a. For $\|\boldsymbol{v}\| > 0$, define the unit velocity direction as

$$\boldsymbol{s}_v = \frac{\boldsymbol{v}}{\|\boldsymbol{v}\|}. \tag{15}$$

The angle between the apparent line of sight and the spacecraft velocity is

$$\tan\theta_{\text{obs}}^{(a)} = \frac{\|\boldsymbol{u}_{I,\text{obs}}^{(a)} \times \boldsymbol{s}_v\|}{\boldsymbol{u}_{I,\text{obs}}^{(a)\top}\boldsymbol{s}_v}, \tag{16}$$

and the aberration angle is

$$\tan\varepsilon^{(a)} = \frac{(\|\boldsymbol{v}\|/c)\sin\theta_{\text{obs}}^{(a)}}{1-(\|\boldsymbol{v}\|/c)\cos\theta_{\text{obs}}^{(a)}}, \tag{17}$$

where c is the speed of light. With

$$\theta_{\text{true}}^{(a)} = \theta_{\text{obs}}^{(a)} + \varepsilon^{(a)},$$

the corresponding geometric inertial direction is

$$\boldsymbol{u}_{I,\text{true}}^{(a)} = \frac{\boldsymbol{u}_{I,\text{obs}}^{(a)}\sin\theta_{\text{true}}^{(a)} - \boldsymbol{s}_v\sin\varepsilon^{(a)}}{\sin\theta_{\text{obs}}^{(a)}}. \tag{18}$$

These equations define the inverse aberration correction

$$\boldsymbol{u}_{I,\text{true}}^{(a)} = \mathcal{D}_{\text{ab}}\left(\boldsymbol{u}_{I,\text{obs}}^{(a)}, \boldsymbol{v}\right). \tag{19}$$

For measurement prediction, the corresponding forward correction is

$$\boldsymbol{u}_{I,\text{obs}}^{(a)} = \mathcal{F}_{\text{ab}}\left(\boldsymbol{u}_{I,\text{true}}^{(a)}, \boldsymbol{v}\right) \triangleq \mathcal{D}_{\text{ab}}\left(\boldsymbol{u}_{I,\text{true}}^{(a)}, -\boldsymbol{v}\right). \tag{20}$$

In the numerical implementation, Eqs. (16) and (17) are evaluated using the equivalent quadrant-preserving atan2 form. For $\|\boldsymbol{v}\| = 0$, the correction reduces to the identity map; when $\sin\theta_{\text{obs}}^{(a)} = 0$, the corresponding collinear limiting direction is used. The aberration geometry is shown in Figure 2.

2.4 Multiplicative Residual on the Unit Sphere

For unit-vector measurements, innovations are formed geometrically rather than by Euclidean subtraction. Let $\hat{\boldsymbol{u}} \in \mathbb{S}^2$ be the predicted direction and $\boldsymbol{y} \in \mathbb{S}^2$ the measurement. The multiplicative residual is [24, 25]

$$\boldsymbol{\varepsilon}_{\text{LOS}}(\hat{\boldsymbol{u}}, \boldsymbol{y}) \triangleq \frac{2(\hat{\boldsymbol{u}} \times \boldsymbol{y})}{1 + \hat{\boldsymbol{u}}^\top \boldsymbol{y}}. \tag{21}$$

If $\alpha = \arccos(\hat{\boldsymbol{u}}^\top \boldsymbol{y})$, then

$$\|\boldsymbol{\varepsilon}_{\text{LOS}}(\hat{\boldsymbol{u}}, \boldsymbol{y})\| = 2\tan\left(\frac{\alpha}{2}\right). \tag{22}$$

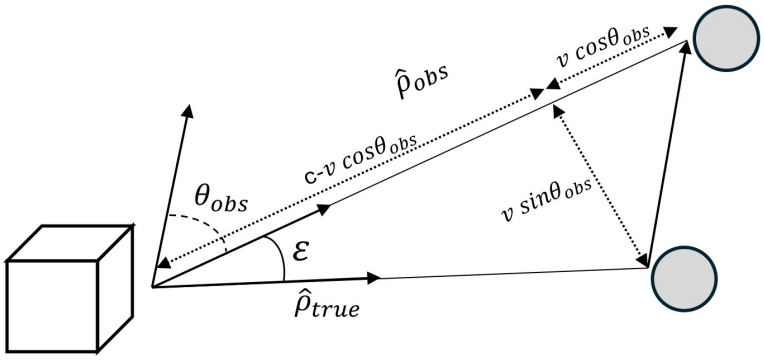


Fig. 2: Geometry of celestial aberration.

Thus, $\boldsymbol{\varepsilon}_{\mathrm{LOS}}$ is a twice-Gibbs representation of the minimum direction error. Since $\hat{\boldsymbol{u}} \times \boldsymbol{y} \perp \hat{\boldsymbol{u}}$, the residual lies in the tangent plane of $\mathbb{S}^2$ at $\hat{\boldsymbol{u}}$ and has two independent components. Let $B(\hat{\boldsymbol{u}}) \in \mathbb{R}^{3\times 2}$ be an orthonormal tangent basis satisfying

$$B(\hat{\boldsymbol{u}})^\top B(\hat{\boldsymbol{u}}) = I_2, \qquad B(\hat{\boldsymbol{u}})^\top \hat{\boldsymbol{u}} = \mathbf{0}_2. \tag{23}$$

The corresponding two-dimensional tangent innovation is

$$\boldsymbol{z} = B(\hat{\boldsymbol{u}})^\top \boldsymbol{\varepsilon}_{\mathrm{LOS}}(\hat{\boldsymbol{u}}, \boldsymbol{y}) \in \mathbb{R}^2. \tag{24}$$

Equation (24) therefore provides a two-dimensional coordinate representation of the same local direction error described by the three-dimensional residual in Eq. (21). The same tangent-plane geometry is used next to compare additive-normalized and multiplicative direction-noise mappings.

3 Geometry of Direction-Measurement Noise on $\mathbb{S}^2$

To isolate this mapping effect from the sensor-noise levels used in the simulations, consider a zero-mean Gaussian perturbation with equal variance in both tangent directions of $\bar{\boldsymbol{u}} \in \mathbb{S}^2$. Let $B(\bar{\boldsymbol{u}}) \in \mathbb{R}^{3\times 2}$ be an orthonormal tangent basis satisfying Eq. (23). Although the estimator uses the three-dimensional rotational-noise model of Eq. (13), a unit vector measurement contains only two independent local directions. For the present geometric comparison, the perturbation is therefore represented in the two-dimensional tangent space as

$$\boldsymbol{\xi} \sim \mathcal{N}\left(\mathbf{0}_2, \sigma^2 I_2\right), \tag{25}$$

with tangent displacement, see Fig. 3a,

$$\boldsymbol{\zeta} = B(\bar{\boldsymbol{u}})\boldsymbol{\xi}, \qquad \varrho = \|\boldsymbol{\zeta}\| = \|\boldsymbol{\xi}\|. \tag{26}$$

To obtain the same noise perturbation in the tangent direction, the additive-normalized mapping is

$$\boldsymbol{y}_A = \frac{\bar{\boldsymbol{u}} + \boldsymbol{\zeta}}{\|\bar{\boldsymbol{u}} + \boldsymbol{\zeta}\|}, \tag{27}$$

whereas the multiplicative mapping is

$$\boldsymbol{y}_M = \exp\left([\bar{\boldsymbol{u}} \times \boldsymbol{\zeta}]_\times\right) \bar{\boldsymbol{u}}. \tag{28}$$

Here, $\boldsymbol{y}_M$ indicates a line-of-sight measurement vector affected by multiplicative noise, while $\boldsymbol{y}_A$ indicates a measurement affected by additive noise and then normalized. Let

$$\theta = \arccos\left(\bar{\boldsymbol{u}}^\top \boldsymbol{y}\right) \tag{29}$$

denote the geodesic cone half-angle from the nominal direction. Since $\boldsymbol{\zeta} \perp \bar{\boldsymbol{u}}$, the two mappings, for additive (A) noise and multiplicative (M) noise, give

$$\theta_A = \arctan \varrho, \qquad \theta_M = \varrho, \tag{30}$$

where the multiplicative relation applies to the principal geodesic branch. Thus, additive normalization compresses the tangent radius and is not representative of a realistic scenario, whereas the multiplicative mapping preserves it as geodesic distance.

For visualization purposes, let us consider the tangent covariance intentionally enlarged to

$$P_\xi = 0.3 \text{ rad}^2 I_2, \qquad \sigma = \sqrt{0.3} \text{ rad} = 0.5477 \text{ rad}, \tag{31}$$

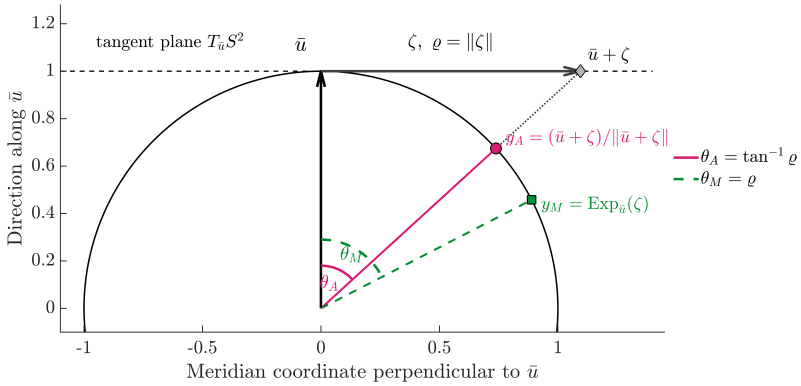
so that the difference between the mappings is visible when represented in Fig. 3. The $k\sigma$ source radii map according to

$$\theta_A(k) = \arctan(k\sigma), \qquad \theta_M(k) = k\sigma, \qquad k = 1, 2, 3. \tag{32}$$

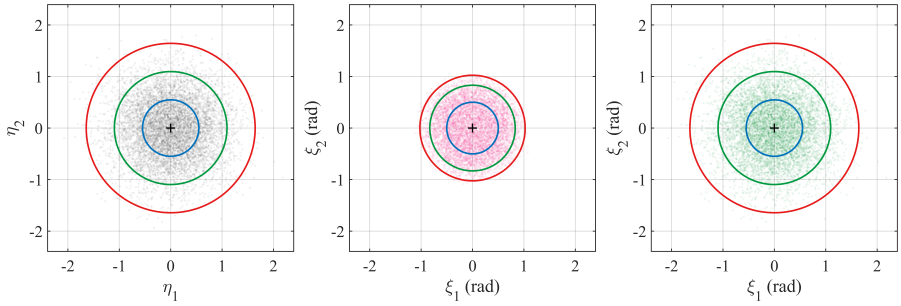
indicates the aperture angle of the cone indicating the noise at one, two, and three standard deviations, respectively. The corresponding additive-normalized cone angles are 0.5011, 0.8309, and 1.0241 rad, while the multiplicative angles are 0.5477, 1.0954, and 1.6432 rad. Thus, additive noise underrepresents the spread of the distribution, especially on the tails of the Gaussian. These values are used only for the geometric illustration of Fig. 3b; the sensor-noise levels used in the Monte Carlo simulations are specified separately.

Figures 3 and 4 show the same effect in spherical and geodesic coordinates: additive normalization shifts the samples toward smaller cone angles, whereas the multiplicative mapping preserves the tangent-space radius as geodesic distance. For the isotropic tangent Gaussian, the radial variable $\varrho = \|\boldsymbol{\xi}\|$ follows the Rayleigh density

$$p_\varrho(\varrho) = \frac{\varrho}{\sigma^2} \exp\left(-\frac{\varrho^2}{2\sigma^2}\right). \tag{33}$$



(a) Meridian-plane comparison of additive-normalized and multiplicative direction-noise mappings.



(b) Tangent-plane samples and mapped directions: source samples (left), additive-normalized mapping (middle), and multiplicative mapping (right).

Fig. 3: Geometric interpretation of direction-measurement noise on $\mathbb{S}^2$.

For the visualization covariance of Eq. (31), the probability of $\varrho \geq \pi$ is approximately 7.18×10^{-8}; this negligible tail is ignored in the following principal-branch comparison. The corresponding cone-angle densities are [42]

$$p_M(\theta) = \frac{\theta}{\sigma^2} \exp\left(-\frac{\theta^2}{2\sigma^2}\right), \qquad 0 \leq \theta < \pi, \tag{34}$$

$$p_A(\theta) = \frac{\tan\theta \, \sec^2\theta}{\sigma^2} \exp\left(-\frac{\tan^2\theta}{2\sigma^2}\right), \qquad 0 \leq \theta < \frac{\pi}{2}. \tag{35}$$

The pointwise densities on the sphere follow from the spherical area element $dA = \sin\theta \, d\theta \, d\phi$. Since both distributions are axisymmetric, it is trivial to derive the probability density of the noisy direction per unit area (solid angle) on the sphere

$$q(\theta) = \frac{p(\theta)}{2\pi \sin\theta}. \tag{36}$$

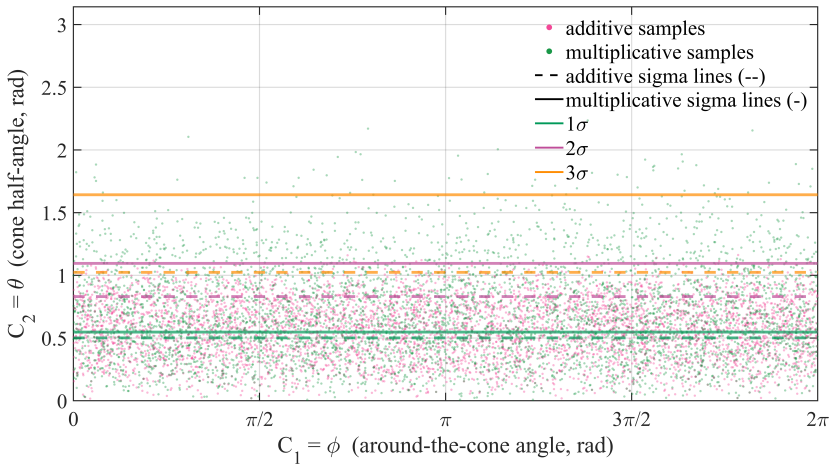


Fig. 4: Unwrapped geodesic representation of the induced spherical samples. The coordinate $C_1 = \phi$ is the azimuth about the nominal direction, and $C_2 = \theta$ is the geodesic cone half-angle.

Therefore, substituting

$$q_M(\theta) = \frac{1}{2\pi\sigma^2} \exp\left(-\frac{\theta^2}{2\sigma^2}\right) \frac{\theta}{\sin\theta}, \tag{37}$$

$$q_A(\theta) = \frac{1}{2\pi\sigma^2} \exp\left(-\frac{\tan^2\theta}{2\sigma^2}\right) \sec^3\theta. \tag{38}$$

As a visualization diagnostic, the pointwise densities are fitted with a Gaussian profile to underline the difference that additive noise brings to the Gaussian assumption during Kalman filtering:

$$\hat{q}_{H,i}(\theta) = A_i \exp\left(-\frac{\theta^2}{2\sigma_{H,i}^2}\right) \quad \text{for} \quad i = \{A, M\}. \tag{39}$$

The fit is obtained over the plotted angular interval and is not used by the estimator. The additive-normalized fit gives $A_A = 0.5973$, $\sigma_{H,A} = 0.5751$ rad, and $\mathrm{RMSE}_A = 4.5932 \times 10^{-2}$, whereas the multiplicative fit gives $A_M = 0.5302$, $\sigma_{H,M} = 0.5785$ rad, and $\mathrm{RMSE}_M = 2.2810 \times 10^{-4}$.

Figure 5 shows the pointwise densities and their Gaussian fits over the full plotted angular interval. The multiplicative density follows the fitted profile closely, while the additive-normalized density departs more strongly as the cone angle increases. To show the fitting discrepancy more clearly, Figure 6 plots the signed error $e_q(\theta) = q(\theta) - \hat{q}_H(\theta)$ on a symmetric-logarithmic scale. The additive-normalized mapping produces a larger structured fitting error, while the multiplicative fit remains close to zero over the same interval.

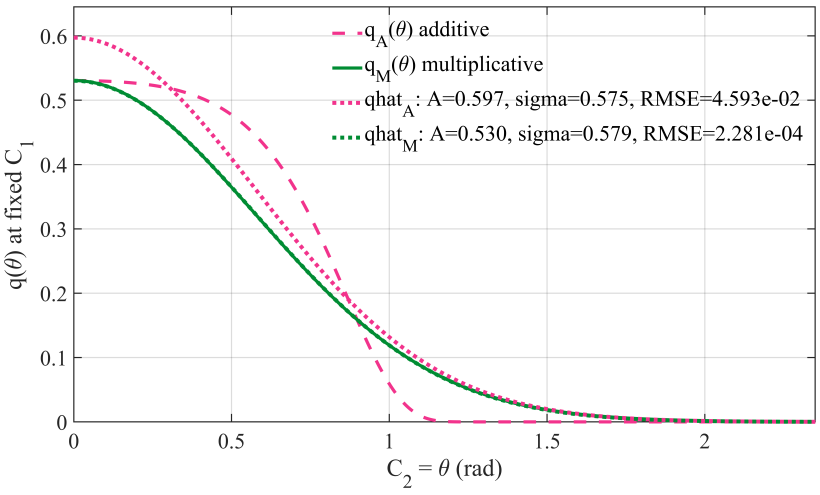


Fig. 5: Pointwise spherical densities and radial Gaussian-like fits for the two direction-noise mappings.

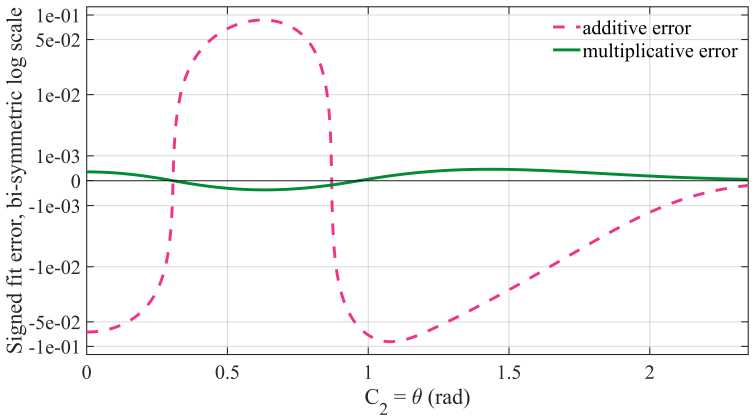


Fig. 6: Signed density-fit error shown on a symmetric-logarithmic scale.

Together, Figures 3–6 show that additive normalization and multiplicative rotation map the same local uncertainty into different spherical distributions. On the principal branch, the multiplicative mapping preserves tangent radius as geodesic distance, whereas additive normalization compresses it according to $\theta_A = \arctan \varrho$. This geometric distinction motivates the multiplicative direction noise model adopted in this work, since additive noise with normalization underestimates the influence of the disturbances.

4 Fully Multiplicative Unscented Kalman Filter

The fully multiplicative unscented Kalman filter (FM-UKF) applies the unscented transformation in the 21-dimensional local error coordinates of Section 2, while retaining the multiplicative attitude and unit-vector measurement geometry [25].

4.1 Time Propagation

Let $\hat{\boldsymbol{x}}_{k-1}^{+}$ and P_{k-1}^{+} denote the posterior nominal state and local error covariance. Using the discrete local process covariance $Q_{d,k-1}$ introduced in Section 2, process uncertainty is included through the augmented covariance

$$P_{\mathrm{aug},k-1}^{+} = \begin{bmatrix} P_{k-1}^{+} & 0 \\ 0 & Q_{d,k-1} \end{bmatrix}. \tag{40}$$

For a covariance $P = C_P C_P^{\top}$ of dimension d, the symmetric $\kappa = 0$ unscented rule used here is

$$\begin{aligned} &\boldsymbol{\Xi}_0 = \mathbf{0}_d, && w_0 = 0, \\ &\boldsymbol{\Xi}_i = \sqrt{d}\, C_P^{(i)}, && \boldsymbol{\Xi}_{i+d} = -\sqrt{d}\, C_P^{(i)}, \qquad w_i = w_{i+d} = \frac{1}{2d}, \end{aligned} \tag{41}$$

for $i = 1, \ldots, d$, where $C_P^{(i)}$ is the ith column of C_P. For prediction, $d = 42$, giving 85 augmented sigma points. Each prediction point is partitioned as

$$\boldsymbol{\Xi}_i^{\mathrm{aug}} = \begin{bmatrix} \boldsymbol{e}_i \\ \boldsymbol{\ell}_i \end{bmatrix}, \qquad \boldsymbol{e}_i, \boldsymbol{\ell}_i \in \mathbb{R}^{21}, \tag{42}$$

where $\boldsymbol{e}_i$ is the local state perturbation and $\boldsymbol{\ell}_i$ is the discrete process-noise perturbation. Each sigma point is propagated as

$$\boldsymbol{x}_k^{(i)} = f_{\Delta t}\left(\hat{\boldsymbol{x}}_{k-1}^{+} \oplus \boldsymbol{e}_i\right) \oplus \boldsymbol{\ell}_i. \tag{43}$$

Thus, the process-noise contribution is already included in the sigma-point spread and is not added again after propagation. The predicted nominal state $\hat{\boldsymbol{x}}_k^{-}$ is obtained by averaging the propagated sigma points on the mixed state space. The Euclidean components $\boldsymbol{\omega}$, $\boldsymbol{b}$, $\boldsymbol{r}$, $\boldsymbol{v}$, $\boldsymbol{\mu}_1$, and $\boldsymbol{\mu}_2$ are averaged algebraically, while the quaternion is averaged using the Markley method [23],

$$M_{q,k} = \sum_i w_i \boldsymbol{q}_k^{(i)} \boldsymbol{q}_k^{(i)\top}, \qquad \hat{\boldsymbol{q}}_k^{-} = \arg\max_{\|\boldsymbol{q}\|=1} \boldsymbol{q}^{\top} M_{q,k} \boldsymbol{q}. \tag{44}$$

After the predicted nominal state is formed, the propagated sigma points are re-centered in the local coordinates,

$$\boldsymbol{e}_k^{(i)} = \boldsymbol{x}_k^{(i)} \ominus \hat{\boldsymbol{x}}_k^{-}, \tag{45}$$

and the predicted covariance is

$$P_k^- = \sum_i w_i \boldsymbol{e}_k^{(i)} \boldsymbol{e}_k^{(i)\top}. \tag{46}$$

4.2 Sequential Measurement Update

At each epoch, the sequential measurement update is initialized with the predicted state and covariance,

$$\bar{\boldsymbol{x}} = \hat{\boldsymbol{x}}_k^-, \qquad \bar{P} = P_k^-. \tag{47}$$

The gyroscope and optical measurements are then processed sequentially. After each update, the resulting pair $(\bar{\boldsymbol{x}}, \bar{P})$ is used as the prior for the next measurement at the same epoch.

4.2.1 Gyroscope Update

For the additive gyroscope measurement of Eq. (11), sigma points are generated from the current 21-dimensional local covariance $\bar{P}$. Because the measurement noise is additive and independent of the state, R_g is added directly to the innovation covariance. Applying Eq. (41) with $d = 21$ gives 43 sigma points. The local points are injected through the retraction of Eq. (4) and transformed as

$$\boldsymbol{Y}_g^{(i)} = \boldsymbol{\omega}^{(i)} + \boldsymbol{b}^{(i)}. \tag{48}$$

Since the gyroscope measurement is affine in $\boldsymbol{\omega}$ and $\boldsymbol{b}$, these sigma-point moments are equivalent to the corresponding linear measurement moments. The predicted measurement, innovation covariance, and state–measurement cross covariance are

$$\hat{\boldsymbol{y}}_g = \sum_i w_i \boldsymbol{Y}_g^{(i)}, \tag{49}$$

$$S_g = \sum_i w_i \left(\boldsymbol{Y}_g^{(i)} - \hat{\boldsymbol{y}}_g\right)\left(\boldsymbol{Y}_g^{(i)} - \hat{\boldsymbol{y}}_g\right)^\top + R_g, \tag{50}$$

$$P_{xg} = \sum_i w_i \boldsymbol{e}_i \left(\boldsymbol{Y}_g^{(i)} - \hat{\boldsymbol{y}}_g\right)^\top. \tag{51}$$

The gain and local correction are

$$K_g = P_{xg} S_g^{-1}, \qquad \delta\hat{\boldsymbol{e}}_g = K_g\left(\boldsymbol{y}_{g,k} - \hat{\boldsymbol{y}}_g\right). \tag{52}$$

The state and covariance are updated as

$$\bar{\boldsymbol{x}} \leftarrow \bar{\boldsymbol{x}} \oplus \delta\hat{\boldsymbol{e}}_g, \qquad \bar{P} \leftarrow \bar{P} - K_g S_g K_g^\top. \tag{53}$$

4.2.2 Unit-Vector Update

For an optical target a observed by tracker j, the current covariance is augmented with the multiplicative rotational-noise covariance,

$$R_{\eta,a} = \sigma_{u,a}^2 I_3, \qquad P_{\mathrm{aug},a} = \begin{bmatrix} \bar{P} & 0 \\ 0 & R_{\eta,a} \end{bmatrix}. \tag{54}$$

Applying Eq. (41) with $d = 24$ gives 49 augmented sigma points, partitioned as

$$\boldsymbol{\Xi}_i^{\mathrm{aug}} = \begin{bmatrix} \boldsymbol{e}_i \\ \boldsymbol{\eta}_i \end{bmatrix}, \qquad \boldsymbol{e}_i \in \mathbb{R}^{21}, \qquad \boldsymbol{\eta}_i \in \mathbb{R}^3. \tag{55}$$

The transformed direction sigma points are

$$\boldsymbol{Y}_i = T(\boldsymbol{\eta}_i) h_{j,a}\left(\bar{\boldsymbol{x}} \oplus \boldsymbol{e}_i\right), \qquad \boldsymbol{Y}_i \in \mathbb{S}^2, \tag{56}$$

where $h_{j,a}(\cdot)$ is the direction measurement model of Eq. (12). The predicted direction $\hat{\boldsymbol{y}} \in \mathbb{S}^2$ is chosen such that the weighted multiplicative residuals are centered at zero,

$$\sum_i w_i \boldsymbol{\varepsilon}_{\mathrm{LOS}}\left(\hat{\boldsymbol{y}}, \boldsymbol{Y}_i\right) = \boldsymbol{0}_3. \tag{57}$$

Using the multiplicative residual of Eq. (21), the sigma-point and measurement residuals are

$$\boldsymbol{Z}_i = \boldsymbol{\varepsilon}_{\mathrm{LOS}}\left(\hat{\boldsymbol{y}}, \boldsymbol{Y}_i\right) = \frac{2(\hat{\boldsymbol{y}} \times \boldsymbol{Y}_i)}{1 + \hat{\boldsymbol{y}}^\top \boldsymbol{Y}_i}, \tag{58}$$

$$\boldsymbol{\nu}_{j,a} = \boldsymbol{\varepsilon}_{\mathrm{LOS}}\left(\hat{\boldsymbol{y}}, \boldsymbol{y}_{j,a}\right) = \frac{2(\hat{\boldsymbol{y}} \times \boldsymbol{y}_{j,a})}{1 + \hat{\boldsymbol{y}}^\top \boldsymbol{y}_{j,a}}. \tag{59}$$

The residual covariance and state–residual cross covariance are

$$P_{zz} = \sum_i w_i \boldsymbol{Z}_i \boldsymbol{Z}_i^\top, \tag{60}$$

$$P_{xz} = \sum_i w_i \boldsymbol{e}_i \boldsymbol{Z}_i^\top. \tag{61}$$

Because the residuals lie in the two-dimensional tangent subspace of $\mathbb{S}^2$, P_{zz} has rank at most two. No additional measurement covariance is added to P_{zz}, because $R_{\eta,a}$ is already represented by the augmented measurement-noise sigma points. The gain and local correction are

$$K_{j,a} = P_{xz} P_{zz}^\dagger, \qquad \delta\hat{\boldsymbol{e}}_{j,a} = K_{j,a} \boldsymbol{\nu}_{j,a}, \tag{62}$$

where $(\cdot)^\dagger$ denotes the pseudoinverse. The state and covariance are updated as

$$\bar{\boldsymbol{x}} \leftarrow \bar{\boldsymbol{x}} \oplus \delta\hat{\boldsymbol{e}}_{j,a}, \qquad \bar{P} \leftarrow \bar{P} - K_{j,a} P_{zz} K_{j,a}^\top. \tag{63}$$

After all measurements at t_k have been processed, the final posterior is

$$\hat{\boldsymbol{x}}_k^+ = \bar{\boldsymbol{x}}, \qquad P_k^+ = \bar{P}. \tag{64}$$

5 Fully Multiplicative Sparse Gauss–Hermite Quadrature Filter

The FM-SGHQF extends the FM-UKF of Section 4 by replacing the unscented integration rule with a Smolyak sparse Gauss–Hermite quadrature rule [36–38]. The state retraction, process-noise augmentation, multiplicative optical-noise model, and sequential measurement structure are retained. The FM-SGHQF uses the same multiplicative direction-residual geometry as the FM-UKF but represents the optical residual by its two independent tangent coordinates. The principal difference in the nonlinear moment transformation is therefore the set of deterministic nodes and weights used in prediction and optical-measurement transformation.

5.1 Sparse Gauss–Hermite Rule

Let d denote the quadrature dimension and let $\boldsymbol{\xi} \sim \mathcal{N}(\mathbf{0}_d, I_d)$. For a scalar- or vector-valued nonlinear mapping g and sparse-grid level L, the corresponding Gaussian expectation is approximated by

$$\mathbb{E}\left[g(\boldsymbol{\xi})\right] \approx \mathcal{A}_{d,L}[g] = \sum_{i=1}^{N_L(d)} w_i^{(L,d)}\, g\left(\boldsymbol{\gamma}_i^{(L,d)}\right), \tag{65}$$

where $\boldsymbol{\gamma}_i^{(L,d)} \in \mathbb{R}^d$ is the ith multidimensional sparse-grid node, $w_i^{(L,d)}$ is its associated quadrature weight, and $N_L(d)$ is the number of distinct nodes after repeated nodes are merged. When the quadrature dimension is clear, the explicit dependence on d is omitted. The multidimensional sparse rule is constructed from one-dimensional Gauss–Hermite rules. To distinguish the one-dimensional level from the multidimensional sparse-grid level L, let ℓ denote the one-dimensional rule level. For a one-dimensional integrand ϕ, define

$$\mathcal{I}_\ell[\phi] = \sum_{r=1}^{m_\ell} \omega_{\ell,r}\, \phi(\chi_{\ell,r}), \qquad m_\ell = 2^\ell - 1, \qquad m_1 = 1, \quad m_2 = 3, \quad m_3 = 7, \tag{66}$$

where $\chi_{\ell,r}$ and $\omega_{\ell,r}$ are the one-dimensional Gauss–Hermite nodes and weights, respectively, scaled for integration with respect to the standard-normal measure.

A conventional d-dimensional Gauss–Hermite rule forms the full tensor product of the one-dimensional rules, using all combinations of the one-dimensional nodes across the d coordinates. A rule with m nodes per dimension therefore requires m^d function evaluations. The Smolyak construction reduces this number by combining only selected tensor products of the one-dimensional rules [36, 38]. For the filter dimensions used

here, $d \geq L$, so the Smolyak operator can be written as

$$\begin{aligned}\mathcal{A}_{d,L}[g] = &\sum_{q=0}^{L-1}(-1)^{L-1-q}\binom{d-1}{L-1-q} \\ &\times \sum_{\substack{\boldsymbol{\alpha}\in\mathbb{N}_+^d \\ \|\boldsymbol{\alpha}\|_1=d+q}} \left(\mathcal{I}_{\alpha_1}\otimes\cdots\otimes\mathcal{I}_{\alpha_d}\right)[g].\end{aligned} \tag{67}$$

Here $\boldsymbol{\alpha} = [\alpha_1, \ldots, \alpha_d]^\top$ is a multi-index, $\mathbb{N}_+ = \{1, 2, \ldots\}$, and $\|\boldsymbol{\alpha}\|_1 = \sum_{j=1}^d \alpha_j$. The operator $\mathcal{I}_{\alpha_1} \otimes \cdots \otimes \mathcal{I}_{\alpha_d}$ denotes the tensor product of the selected one-dimensional quadrature rules. Because every $\alpha_j \geq 1$, the minimum possible value of $\|\boldsymbol{\alpha}\|_1$ is d. Hence $q = \|\boldsymbol{\alpha}\|_1 - d$ represents the total level increment above the all-Level-1 tensor product. Repeated multidimensional nodes are merged by summing their weights. Because the Smolyak construction is a signed combination of tensor-product rules, the resulting sparse-grid weights are not required to be positive.

For the one-dimensional sequence of Eq. (66), the Smolyak rule is guaranteed to integrate multivariate polynomials of total degree up to $2L-1$. Levels 2 and 3 therefore have third- and fifth-degree polynomial exactness, respectively. After repeated nodes are merged, their point counts for $d \geq L$ are

$$N_2(d) = 2d + 1, \qquad N_3(d) = 2d^2 + 6d + 1. \tag{68}$$

In the present filter, the prediction quadrature space has dimension $d_p = 42$, obtained by augmenting the 21-dimensional local state error with the 21-dimensional discrete process-noise error. For each optical measurement update, the quadrature dimension is $d_m = 24$, consisting of the 21-dimensional local state error and the three-dimensional rotational measurement-noise error. The corresponding numbers of sparse-grid nodes are

$$\begin{aligned} N_{2,p} &= 85, & N_{3,p} &= 3781, \\ N_{2,m} &= 49, & N_{3,m} &= 1297, \end{aligned} \tag{69}$$

where the subscripts p and m denote prediction and optical measurement transformations, respectively. For the one- and three-point Level 1 and Level 2 univariate rules of Eq. (66), the resulting Level 2 SGHQ rule is identical to the symmetric unscented rule with

$$\kappa = 3 - d. \tag{70}$$

The FM-UKF of Section 4 instead uses $\kappa = 0$. The two methods therefore use the same $2d + 1$ point locations in number, but not the same locations or weights. Moreover, the central FM-UKF point has zero weight. Figure 7 illustrates this distinction in two dimensions and shows the additional nodes introduced by the Level 3 sparse rule. For the FM-UKF with $\kappa = 0$, the point locations are the origin and $\pm\sqrt{2}\,\boldsymbol{e}_1$, $\pm\sqrt{2}\,\boldsymbol{e}_2$, with zero weight at the origin and weight $1/4$ at each noncentral point. The Level 2 SGHQ rule uses the origin and $\pm\sqrt{3}\,\boldsymbol{e}_1$, $\pm\sqrt{3}\,\boldsymbol{e}_2$, with weights $1/3$ and $1/6$, respectively. The Level 3 rule contains 21 nodes in two dimensions and has fifth-degree rather than third-degree total polynomial exactness. These two-dimensional sets are

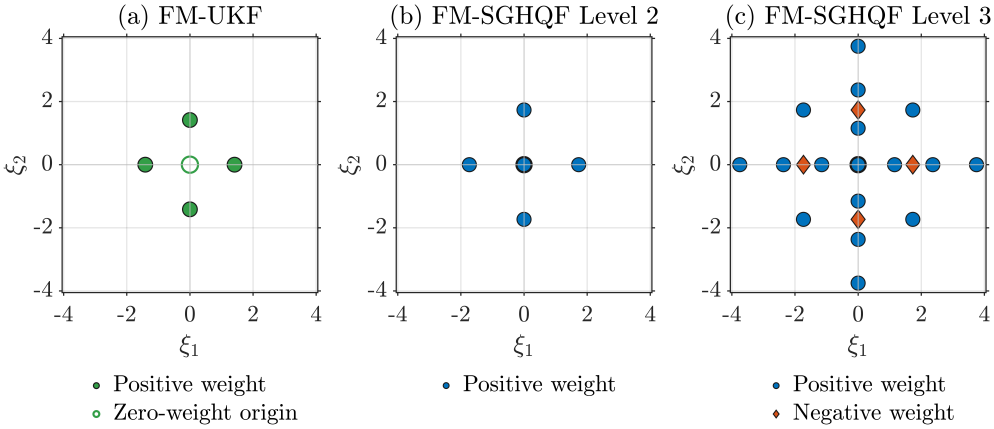


Fig. 7: Two-dimensional comparison of the deterministic quadrature sets.

shown only for visualization; the estimator applies the same quadrature constructions in the 42-dimensional augmented prediction space and the 24-dimensional augmented optical-measurement space.

5.2 Fully Multiplicative SGHQ Construction

5.2.1 Prediction

For prediction, the FM-SGHQF uses the same 42-dimensional augmented state–process covariance as the FM-UKF in Eq. (40). Let

$$P^{+}_{\mathrm{aug},k-1} = S^{p}_{\mathrm{aug},k-1} S^{p\top}_{\mathrm{aug},k-1}. \tag{71}$$

In the numerical implementation, $S^{p}_{\mathrm{aug},k-1}$ is obtained from an SVD-based covariance square root. The Level-L sparse-grid nodes are mapped into the augmented local coordinates as

$$\begin{bmatrix} \boldsymbol{e}^{(i)}_{k-1} \\ \boldsymbol{\ell}^{(i)}_{k-1} \end{bmatrix} = S^{p}_{\mathrm{aug},k-1} \boldsymbol{\gamma}^{(L)}_{i}, \qquad i = 1, \ldots, N_{L,p}, \tag{72}$$

where $\boldsymbol{e}^{(i)}_{k-1}, \boldsymbol{\ell}^{(i)}_{k-1} \in \mathbb{R}^{21}$ are the local state and discrete process-noise perturbations, respectively. Each state perturbation is injected through the retraction, propagated through the nonlinear dynamics, and followed by injection of the corresponding process-noise perturbation, as in Eq. (43).

The predicted nominal state is obtained from the propagated quadrature points using the sparse-grid weights $w^{(L)}_{i}$. Euclidean state components are averaged algebraically, while the quaternion is obtained using the eigenvector-based averaging construction of Eq. (44) with the sparse-grid weights. The propagated points are then re-centered through $\ominus$, and the predicted local covariance is formed from the weighted outer products of the resulting local errors. Because $Q_{d,k-1}$ is already represented by the augmented process-noise quadrature coordinates, it is not added again after propagation.

5.2.2 Sequential Measurement Update

The sequential update begins from the predicted pair $(\hat{\boldsymbol{x}}_k^-, P_k^-)$, as in Eq. (47). The gyroscope model is affine in $\boldsymbol{\omega}$ and $\boldsymbol{b}$, so its Gaussian moments are obtained exactly from the corresponding linear measurement model. The FM-SGHQF therefore applies the linear gyroscope update with covariance R_g.

For an optical target a observed by tracker j, the local state covariance is augmented with the three-dimensional rotational measurement-noise covariance of Eq. (54). Let

$$P_{\mathrm{aug},a} = S^m_{\mathrm{aug},a} S^{m\top}_{\mathrm{aug},a}. \tag{73}$$

The corresponding Level-L quadrature coordinates are

$$\begin{bmatrix} \boldsymbol{e}_i \\ \boldsymbol{\eta}_i \end{bmatrix} = S^m_{\mathrm{aug},a} \boldsymbol{\gamma}_i^{(L)}, \qquad i = 1, \ldots, N_{L,m}, \tag{74}$$

where $\boldsymbol{e}_i \in \mathbb{R}^{21}$ and $\boldsymbol{\eta}_i \in \mathbb{R}^3$. Each pair is transformed through the multiplicative optical model,

$$\boldsymbol{Y}_i = T(\boldsymbol{\eta}_i) h_{j,a}\left(\bar{\boldsymbol{x}} \oplus \boldsymbol{e}_i\right). \tag{75}$$

The predicted direction is obtained using the same multiplicative mean condition as in Eq. (57), with the unscented weights replaced by the sparse-grid weights $w_i^{(L)}$. For each transformed direction $\boldsymbol{Y}_i$, the three-dimensional multiplicative residual is

$$\boldsymbol{\varepsilon}_i = \boldsymbol{\varepsilon}_{\mathrm{LOS}}\left(\hat{\boldsymbol{y}}, \boldsymbol{Y}_i\right) = \frac{2\left(\hat{\boldsymbol{y}} \times \boldsymbol{Y}_i\right)}{1 + \hat{\boldsymbol{y}}^\top \boldsymbol{Y}_i}. \tag{76}$$

Similarly, the residual associated with the measured direction $\boldsymbol{y}_{j,a}$ is

$$\boldsymbol{\varepsilon}_a = \boldsymbol{\varepsilon}_{\mathrm{LOS}}\left(\hat{\boldsymbol{y}}, \boldsymbol{y}_{j,a}\right) = \frac{2\left(\hat{\boldsymbol{y}} \times \boldsymbol{y}_{j,a}\right)}{1 + \hat{\boldsymbol{y}}^\top \boldsymbol{y}_{j,a}}. \tag{77}$$

Both residuals lie in the two-dimensional tangent space of $\mathbb{S}^2$ at $\hat{\boldsymbol{y}}$. Using the orthonormal tangent basis $B(\hat{\boldsymbol{y}})$ of Eq. (23), the residual coordinates used in the FM-SGHQF update are

$$\boldsymbol{z}_i = B(\hat{\boldsymbol{y}})^\top \boldsymbol{\varepsilon}_i, \tag{78}$$

$$\boldsymbol{\nu}_a = B(\hat{\boldsymbol{y}})^\top \boldsymbol{\varepsilon}_a. \tag{79}$$

Thus, $\boldsymbol{z}_i, \boldsymbol{\nu}_a \in \mathbb{R}^2$. The corresponding residual covariance and state–residual cross covariance are

$$P_{zz} = \sum_{i=1}^{N_{L,m}} w_i^{(L)} \boldsymbol{z}_i \boldsymbol{z}_i^\top, \tag{80}$$

$$P_{xz} = \sum_{i=1}^{N_{L,m}} w_i^{(L)} \boldsymbol{e}_i \boldsymbol{z}_i^\top. \tag{81}$$

Since the residual is represented directly in its two independent tangent coordinates, $P_{zz} \in \mathbb{R}^{2\times 2}$. The gain and local correction are

$$K_a = P_{xz} P_{zz}^{-1}, \qquad \delta\hat{\boldsymbol{e}}_a = K_a \boldsymbol{\nu}_a. \tag{82}$$

No additional optical measurement covariance is added because $\sigma_{u,a}^2 I_3$ is already represented by the augmented measurement-noise quadrature coordinates. The correction is applied through the same retraction and covariance update as the FM-UKF before processing the next measurement.

6 MEKF Comparison Baseline

The MEKF is retained only as a first-order comparison baseline [15, 16]. It uses the same 21-dimensional local-error state, nonlinear dynamics, stochastic model, tracker-calibration states, measurement sequence, and optical measurement geometry defined in Section 2. The attitude correction is applied through the right-multiplicative retraction of Eq. (4).

For the MEKF, the nominal state is propagated through the nonlinear dynamics, while the local covariance is propagated using the time-varying Jacobian $F_c(\hat{\boldsymbol{x}}(t))$ of the continuous local-error dynamics evaluated along the nominal trajectory,

$$\dot{P} = F_c(\hat{\boldsymbol{x}}(t))\, P + P F_c^{\top}(\hat{\boldsymbol{x}}(t)) + Q_c. \tag{83}$$

Here Q_c is the continuous-time local process-noise spectral-density matrix expressed in the 21-dimensional local-error coordinates and corresponds to the same stochastic model used to obtain $Q_{d,k-1}$ for the nonlinear filters. The process-noise amplitudes are given in Table 1. Equation (83) is integrated using the same internal propagation substeps as the nominal dynamics, with F_c evaluated along the propagated nominal trajectory rather than held fixed over the complete estimator-cycle interval.

The gyroscope and optical measurements are processed sequentially using first-order sensitivities of the common measurement models. For each measurement, the local measurement model is

$$\boldsymbol{z}_a \approx H_a \boldsymbol{e} + \boldsymbol{n}_a, \qquad H_a = \left.\frac{\partial \boldsymbol{z}_a}{\partial \boldsymbol{e}}\right|_{\boldsymbol{e}=\boldsymbol{0}}, \qquad \boldsymbol{n}_a \sim \mathcal{N}(\boldsymbol{0}, R_a). \tag{84}$$

For an optical direction, $\boldsymbol{z}_a$ is the two-dimensional tangent innovation of Eq. (24); the gyroscope uses the Euclidean measurement model of Eq. (11). The resulting local correction is applied through the retraction of Eq. (4).

7 Numerical Simulations and Results

The four estimators are evaluated using common Monte Carlo truth, initial-condition, process-noise, and measurement realizations. At each estimator epoch, the measurement set contains one three-component gyroscope measurement and eight optical unit-vector measurements. Tracker 1 provides three identified stellar directions and

Table 1: Common estimator initialization and stochastic parameters.

Quantity	Symbol	Value
Attitude prior standard deviation	$\sigma_{\delta\theta,0}$	0.20° per axis
Angular-rate prior standard deviation	$\sigma_{\delta\omega,0}$	5×10^{-3} rad/s per axis
Gyroscope-bias prior standard deviation	$\sigma_{\delta b,0}$	5×10^{-5} rad/s per axis
Position prior standard deviation	$\sigma_{\delta r,0}$	25 km per axis
Velocity prior standard deviation	$\sigma_{\delta v,0}$	2.0×10^{-2} km/s per axis
Angular-rate process-noise amplitude	$\sigma_{\dot{\omega}}$	5×10^{-7} rad $\mathrm{s}^{-3/2}$
Bias process-noise amplitude	$\sigma_{\dot{b}}$	5×10^{-8} rad $\mathrm{s}^{-3/2}$
Translational process-noise amplitude	σ_a	5×10^{-11} km $\mathrm{s}^{-3/2}$
Misalignment process-noise amplitude	$\sigma_{\dot{\mu}_1}$, $\sigma_{\dot{\mu}_2}$	10^{-14} rad $\mathrm{s}^{-1/2}$
Gyroscope measurement standard deviation	σ_g	10^{-4} rad/s
Stellar-direction standard deviation	σ_s	5 arcsec
Celestial-body direction standard deviation	σ_p	10 arcsec

one Moon line-of-sight measurement, while tracker 2 provides three identified stellar directions and one Mars line-of-sight measurement. The celestial-body observations pass through the same tracker mounting and residual misalignment as the stellar observations from the corresponding tracker. Each optical unit vector contributes two independent tangent-space components.

7.1 Simulation Scenario and Numerical Implementation

The numerical study uses an Earth-centered two-body orbit model with $\mu_g = 398600.4418$ $\mathrm{km}^3/\mathrm{s}^2$ and torque-free rigid-body attitude dynamics, with $J = \mathrm{diag}(0.1625, 0.1625, 0.1)$ $\mathrm{kg\,m}^2$. The nominal truth state is initialized as

$$\begin{aligned} &\boldsymbol{r}_0 = [7000,\, 0,\, 0]^\top \text{ km}, && \boldsymbol{v}_0 = [0,\, \sqrt{\mu_g/7000},\, 0]^\top \text{ km/s}, \\ &\boldsymbol{q}_0 = [0,\, 0,\, 0,\, 1]^\top, && \boldsymbol{\omega}_0 = [0.020,\, 0.014,\, -0.016]^\top \text{ rad/s}, \\ &\boldsymbol{b}_0 = [1,\, -2,\, 1]^\top \times 10^{-4} \text{ rad/s}. \end{aligned} \tag{85}$$

The two optical trackers follow the measurement model of Section 2.2, with tracker 1 nominally aligned with the body frame and tracker 2 mounted 90° about the body y axis. Each tracker observes three fixed stellar directions and one celestial body. Celestial aberration is included in both truth generation and measurement prediction.

The common estimator initialization and stochastic parameters are listed in Table 1, with the joint tracker-misalignment prior given in Appendix A. Two $N_{\mathrm{MC}} = 100$ Monte Carlo cases are considered: $\Delta t = 0.5$ s and $\Delta t = 90$ s, both with a requested duration of 50 000 s. The coarse-step case is used as a numerical stress test in which the longer propagation interval and lower measurement-update frequency increase the effect of nonlinear uncertainty transformation.

7.2 Accuracy and Statistical Consistency

Figures 8 and 9 compare the filter-predicted uncertainty with the empirical Monte Carlo dispersion. Agreement between the two indicates that the reported covariance is representative of the observed estimation error, whereas systematic underprediction indicates overconfidence. For $\Delta t = 0.5$ s, all four estimators exhibit close predicted–empirical agreement. Position and velocity uncertainty decrease after initialization, while the attitude, gyroscope-bias, and tracker-misalignment errors remain bounded. At this estimator-cycle interval, the differences among the uncertainty transformations are small, and the first-order covariance approximation used by the MEKF remains adequate for the investigated initial uncertainty.

At $\Delta t = 90$ s, the estimator behavior separates more clearly. The FM-UKF and Level 3 FM-SGHQF maintain close agreement between the predicted uncertainty and empirical Monte Carlo dispersion. The Level 2 FM-SGHQF remains bounded, but its predicted covariance becomes substantially smaller than the observed state-error dispersion, particularly for attitude and tracker misalignment. The MEKF also remains bounded but exhibits substantially larger estimation errors and a pronounced mismatch between its predicted covariance and the empirical dispersion. Thus, the coarse-step MEKF result is characterized by reduced accuracy and covariance inconsistency rather than numerical divergence.

For state group $g \in \{r, v, \delta\theta, b, \mu_1, \mu_2\}$, the Monte Carlo group RMSE is

$$\mathrm{RMSE}_{g,k} = \left[\frac{1}{N_{\mathrm{MC}}} \sum_{m=1}^{N_{\mathrm{MC}}} \left\| \boldsymbol{e}_{g,k}^{(m)} \right\|_2^2 \right]^{1/2}, \tag{86}$$

where $\boldsymbol{e}_{\delta\theta,k}^{(m)} \equiv \delta\boldsymbol{\theta}_k^{(m)}$ is the local multiplicative attitude error, and the remaining group errors are the corresponding Euclidean components of $\boldsymbol{x}_k^{(m)} \ominus \hat{\boldsymbol{x}}_k^{(m)}$. Figure 10 shows the corresponding error histories for the coarse-step case. The FM-UKF and Level 3 FM-SGHQF remain closely matched. The Level 2 FM-SGHQF has larger position, velocity, attitude, and tracker-misalignment errors, while the MEKF errors remain substantially larger than those of the three nonlinear filters. At the final simulated epoch, the MEKF, FM-UKF, Level 2 FM-SGHQF, and Level 3 FM-SGHQF give position RMSEs of 80.22, 2.974, 7.988, and 2.902 km, respectively. The corresponding attitude RMSEs are 0.8161, 1.093×10^{-2}, 5.759×10^{-2}, and 1.062×10^{-2} deg. The complete final-epoch results are reported in Table 2.

Filter consistency is evaluated using the normalized innovation squared (NIS) and normalized estimation error squared (NEES) [43, 44]. Since the measurements are processed sequentially, the epoch-level NIS is

$$\mathrm{NIS}_k^{(m)} = \sum_{a \in \mathcal{M}_k} \boldsymbol{\nu}_{a,k}^{(m)\top} S_{a,k}^{(m)\dagger} \boldsymbol{\nu}_{a,k}^{(m)}, \tag{87}$$

where $S^\dagger$ denotes the inverse when S is full rank and the pseudoinverse for the rank-two FM-UKF optical update. With one three-component gyroscope measurement and eight optical directions, each contributing two independent components, the expected

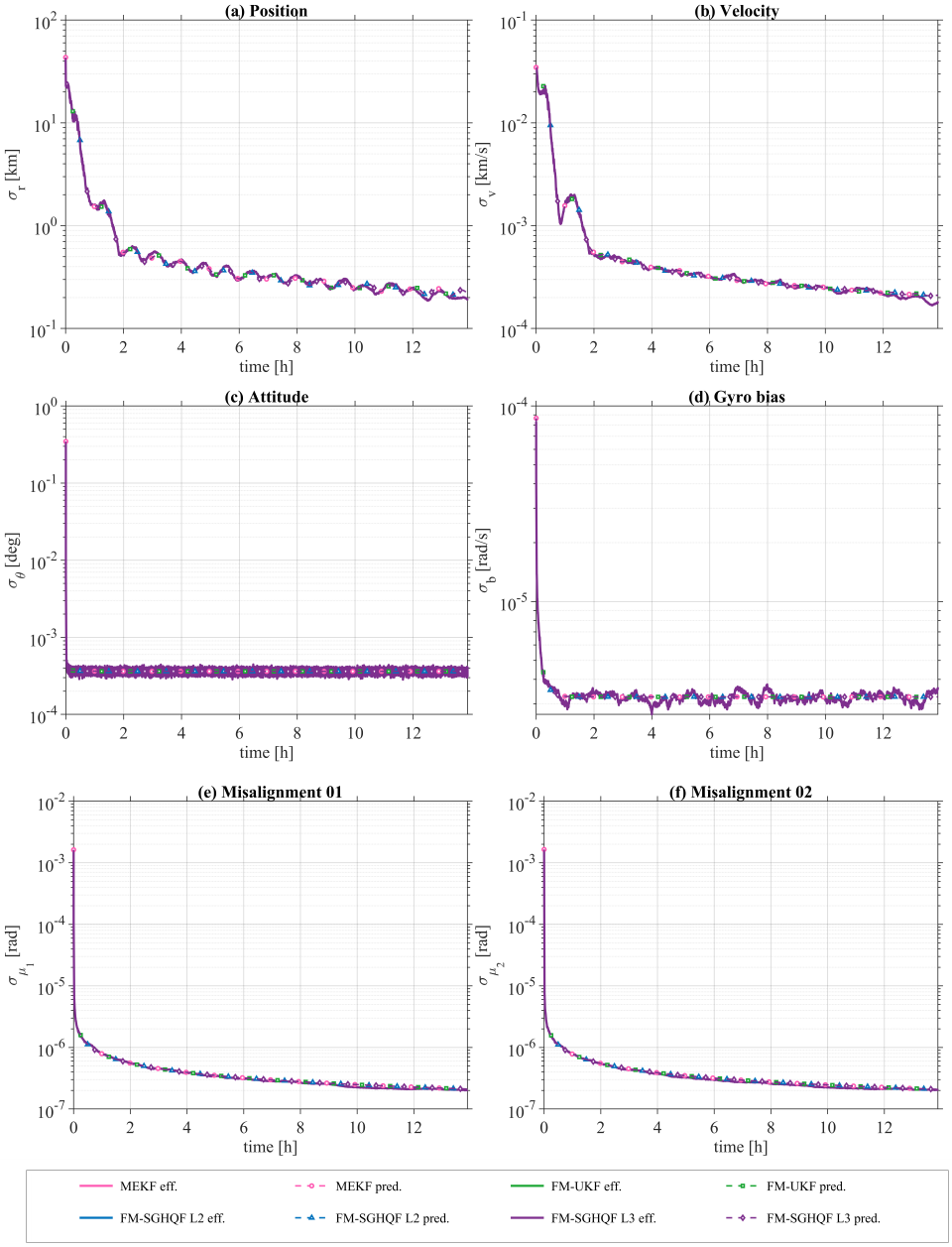


Fig. 8: Predicted and empirical state-group standard deviations for $\Delta t = 0.5$ s: (a) position, (b) velocity, (c) attitude, (d) gyroscope bias, (e) $\boldsymbol{\mu}_1$, and (f) $\boldsymbol{\mu}_2$.

Table 2: Final group RMSE at $t = 49\,950$ s for $\Delta t = 90$ s and 100 Monte Carlo realizations.

State group	MEKF	FM-UKF	FM-SGHQF L2	FM-SGHQF L3	Unit
Position, $\boldsymbol{r}$	8.022×10^{1}	2.974	7.988	2.902	km
Velocity, $\boldsymbol{v}$	7.998×10^{-2}	3.067×10^{-3}	6.513×10^{-3}	3.032×10^{-3}	km/s
Attitude, $\delta\boldsymbol{\theta}$	8.161×10^{-1}	1.093×10^{-2}	5.759×10^{-2}	1.062×10^{-2}	deg
Gyroscope bias, $\boldsymbol{b}$	2.434×10^{-5}	1.170×10^{-5}	1.170×10^{-5}	1.170×10^{-5}	rad/s
Misalignment, $\boldsymbol{\mu}_1$	1.424×10^{-2}	1.879×10^{-4}	1.002×10^{-3}	1.825×10^{-4}	rad
Misalignment, $\boldsymbol{\mu}_2$	1.424×10^{-2}	1.880×10^{-4}	1.003×10^{-3}	1.826×10^{-4}	rad

NIS is 19. State consistency is evaluated using the degrees-of-freedom-normalized NEES,

$$\mathrm{NEES}_k^{(m),\mathrm{norm}} = \frac{1}{n_x} \boldsymbol{e}_k^{(m)\top} \left(P_k^{(m)}\right)^{-1} \boldsymbol{e}_k^{(m)}, \qquad n_x = 21. \tag{88}$$

The corresponding average normalized estimation error squared (ANEES) is

$$\mathrm{ANEES}_k^{\mathrm{norm}} = \frac{1}{N_{\mathrm{MC}}} \sum_{m=1}^{N_{\mathrm{MC}}} \mathrm{NEES}_k^{(m),\mathrm{norm}}. \tag{89}$$

Under the assumed stochastic model, both normalized statistics have an expected value of unity.

Figures 11 and 12 show the measurement- and state-consistency behavior for the coarse-step case. The FM-UKF and Level 3 FM-SGHQF remain close to the expected NIS and ANEES levels after the initial transient. The Level 2 FM-SGHQF also maintains an NIS near the expected measurement level, but its ANEES remains approximately two orders of magnitude above unity over the latter portion of the simulation. Its measurement innovations are therefore substantially better represented than its full-state estimation error, consistent with the predicted–empirical covariance mismatch in Figure 9.

The MEKF remains bounded but exhibits a different consistency behavior. Its mean NIS remains above the expected value, while its normalized ANEES is several orders of magnitude greater than unity over much of the simulation. The same mismatch is visible in Figure 9, where the empirical attitude and tracker-misalignment dispersion remains substantially larger than the corresponding MEKF-predicted uncertainty.

That is, these results prove that the proposed filters are more robust and show a higher level of consistency, both internal regarding the measurement prediction, and external regarding the filters' own estimation of the spread of the error.

7.3 Computational Cost and Estimator Selection

All computation times were measured on an 11th Gen Intel® Core™ i7-11370H processor at 3.30 GHz with 16 GB of RAM, using MATLAB R2024b on Windows 11

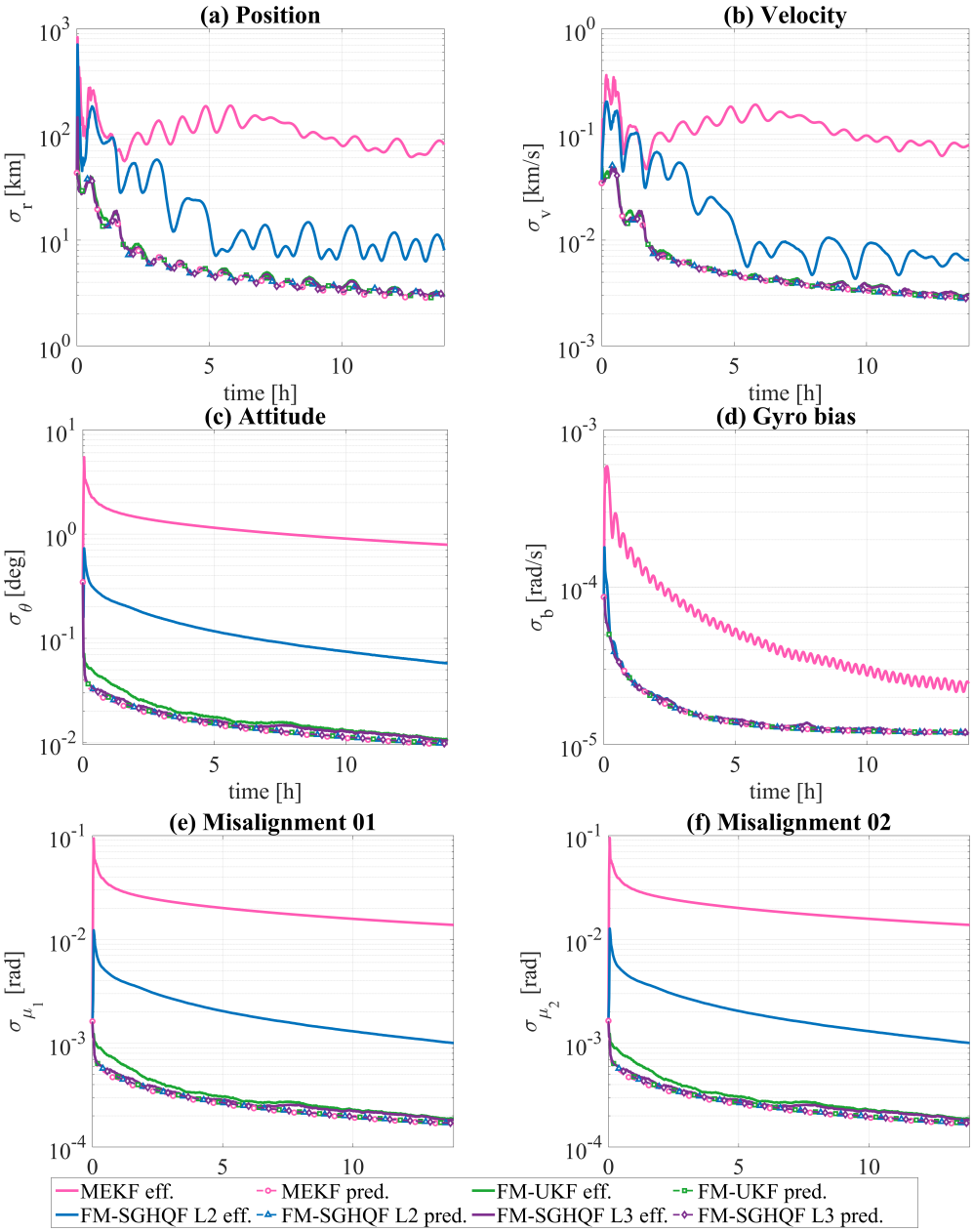


Fig. 9: Predicted and empirical state-group standard deviations for $\Delta t = 90$ s: (a) position, (b) velocity, (c) attitude, (d) gyroscope bias, (e) tracker-1 misalignment, and (f) tracker-2 misalignment.

Home 64-bit. The reported values are mean wall-clock computation times per estimator epoch.

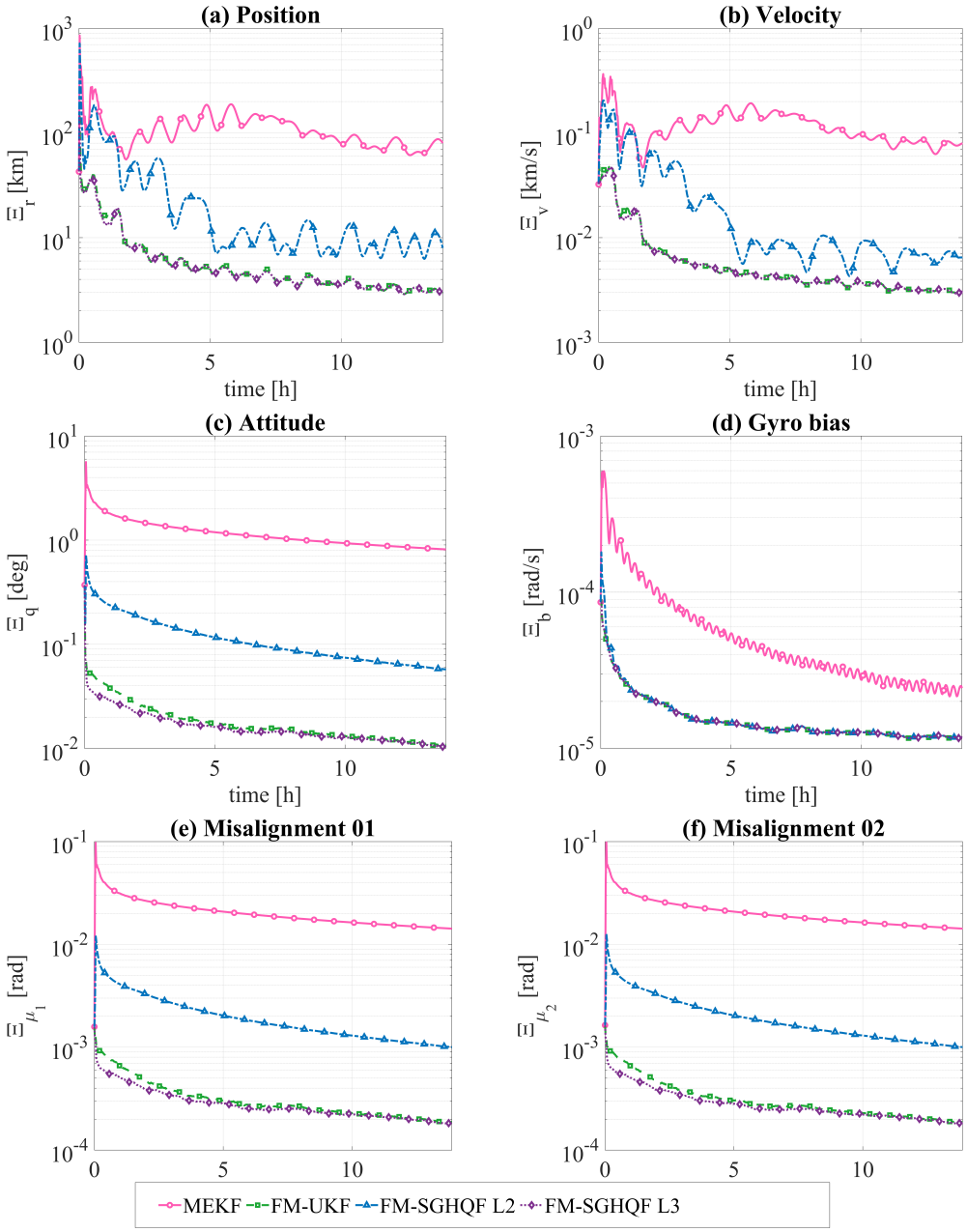


Fig. 10: Monte Carlo group RMSE for $\Delta t = 90$ s: (a) position, (b) velocity, (c) attitude, (d) gyroscope bias, (e) $\boldsymbol{\mu}_1$, and (f) $\boldsymbol{\mu}_2$.

Figure 13 compares the mean computation time per estimator epoch. At $\Delta t = 0.5$ s, the mean runtimes are 1.87×10^{-3}, 6.99×10^{-2}, 3.97×10^{-2}, and 8.40×10^{-1} s for the

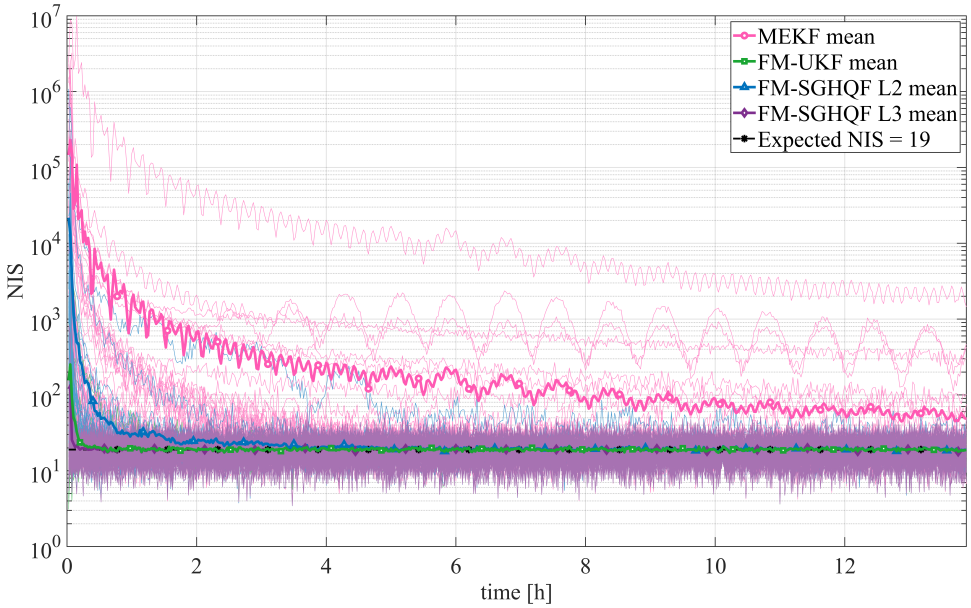


Fig. 11: Raw epoch-level NIS histories for $\Delta t = 90$ s. Thin curves denote individual Monte Carlo realizations, thick curves denote the Monte Carlo means, and the dashed horizontal line denotes the expected raw NIS, $n_z = 19$.

MEKF, FM-UKF, FM-SGHQF Level 2, and FM-SGHQF Level 3, respectively. Only Level 3 exceeds the 0.5 s estimator-cycle interval.

At $\Delta t = 90$ s, the corresponding mean runtimes are 2.71×10^{-2}, 2.58×10^{-1}, 2.59×10^{-1}, and 10.8 s, respectively. All four remain below the 90 s estimator-cycle interval. The FM-UKF and Level 2 FM-SGHQF have nearly identical mean computational cost in this case. Level 3 requires approximately 42 times the FM-UKF runtime. Although Level 3 gives coarse-step accuracy and covariance-consistency behavior close to the FM-UKF, this improvement is obtained at substantially greater computational cost. Level 2 provides essentially no computational advantage over the FM-UKF in the coarse-step case while giving larger state errors and substantially underestimating the full-state uncertainty.

Table 3 summarizes the predicted–empirical covariance agreement and timing feasibility of the four estimators. At $\Delta t = 0.5$ s, all four estimators retain close predicted–empirical covariance agreement. At $\Delta t = 90$ s, the FM-UKF and Level 3 FM-SGHQF retain this agreement, whereas the MEKF and Level 2 FM-SGHQF do not. The coarse-step NIS and ANEES results provide the corresponding innovation- and state-consistency diagnostics. The Level 3 mean runtime exceeds the 0.5 s estimator-cycle interval in the fine-step case. The FM-UKF is therefore the only estimator satisfying both covariance and timing criteria at both investigated estimator-cycle intervals.

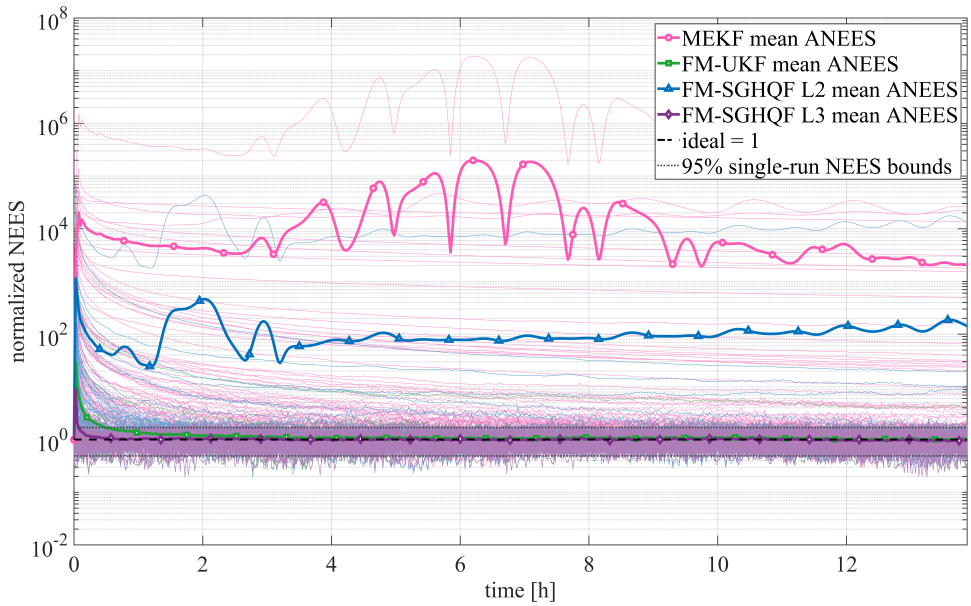
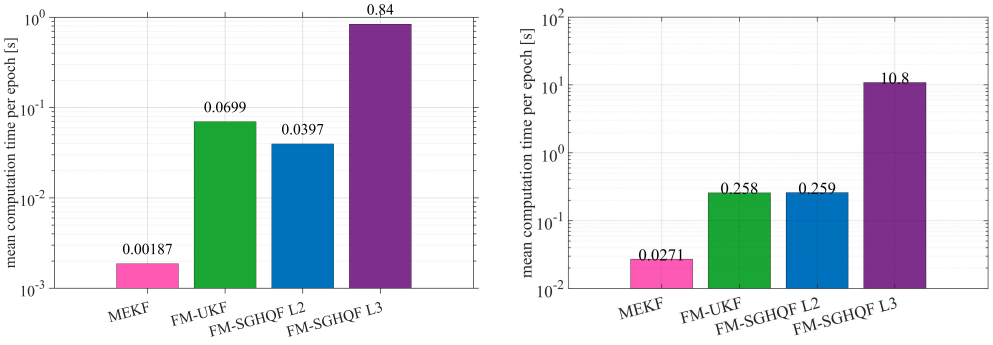


Fig. 12: Normalized NEES histories for $\Delta t = 90$ s. Thin curves denote individual Monte Carlo realizations and thick curves denote the normalized ANEES for each estimator. The dashed line denotes the expected value of unity, and the dotted lines denote the 95% single-realization normalized-NEES bounds.



(a) $\Delta t = 0.5$ s (b) $\Delta t = 90$ s

Fig. 13: Mean computation time per estimator epoch for the four estimators at the two estimator-cycle intervals.

Because the FM-UKF is the only estimator satisfying both criteria across the two investigated estimator-cycle intervals, its covariance behavior is examined at the state-group level as a final diagnostic. For $g \in \{r, v, \delta\theta, b, \mu_1, \mu_2\}$, define the error norm for

Table 3: Summary of predicted–empirical covariance agreement and mean timing feasibility.

Estimator	NIS/ANEES near expected levels		Mean runtime $< \Delta t$		Both conditions
	0.5 s	90 s	0.5 s	90 s	in both cases
MEKF	✓	×	✓	✓	×
FM-UKF	✓	✓	✓	✓	✓
FM-SGHQF L2	✓	×	✓	✓	×
FM-SGHQF L3	✓	✓	×	✓	×

Monte Carlo realization m and its ensemble mean as

$$d_{g,k}^{(m)} = \left\| \boldsymbol{e}_{g,k}^{(m)} \right\|_2, \qquad \bar{d}_{g,k} = \frac{1}{N_{\mathrm{MC}}} \sum_{m=1}^{N_{\mathrm{MC}}} d_{g,k}^{(m)}. \tag{90}$$

The corresponding predicted and empirical group uncertainty scales are

$$\sigma_{g,k}^{\mathrm{pred}} = \sqrt{\frac{1}{N_{\mathrm{MC}}} \sum_{m=1}^{N_{\mathrm{MC}}} \mathrm{tr}\left(P_{gg,k}^{(m)}\right)}, \qquad \sigma_{g,k}^{\mathrm{emp}} = \sqrt{\mathrm{tr}\left(\widehat{C}_{g,k}\right)}, \tag{91}$$

where $P_{gg,k}^{(m)}$ is the covariance submatrix associated with state group g, and $\widehat{C}_{g,k}$ is the empirical covariance of the corresponding Monte Carlo errors.

Figure 14 compares the individual Monte Carlo error norms and their ensemble mean with $3\sigma_{g,k}^{\mathrm{pred}}$ and $3\sigma_{g,k}^{\mathrm{emp}}$. The predicted and empirical uncertainty scales remain close for position, velocity, attitude, gyroscope bias, and both tracker-misalignment states over the coarse-step simulation. This state-group behavior is consistent with the FM-UKF NIS and ANEES results of Section 7.2 and provides an additional check that its reported covariance remains representative across the estimated state groups.

Taken together, the coarse-step accuracy, NIS/ANEES behavior, computational cost, and state-group covariance diagnostic identify the FM-UKF as the estimator carried forward for subsequent image-level and hardware-in-the-loop evaluation of the optical-navigation architecture.

8 Conclusion

The proposed study compared four estimators for joint spacecraft attitude–orbit estimation with simultaneous calibration of two optical-tracker misalignments: an MEKF, an FM-UKF, and FM-SGHQFs at sparse-grid Levels 2 and 3. All the filters shared the same dynamics, state, stochastic model, and multiplicative unit-vector measurement model. After showing that multiplicative noise yields a more realistic simulation than the commonly used additive case, the multiplicative filters showed greater robustness and consistency.

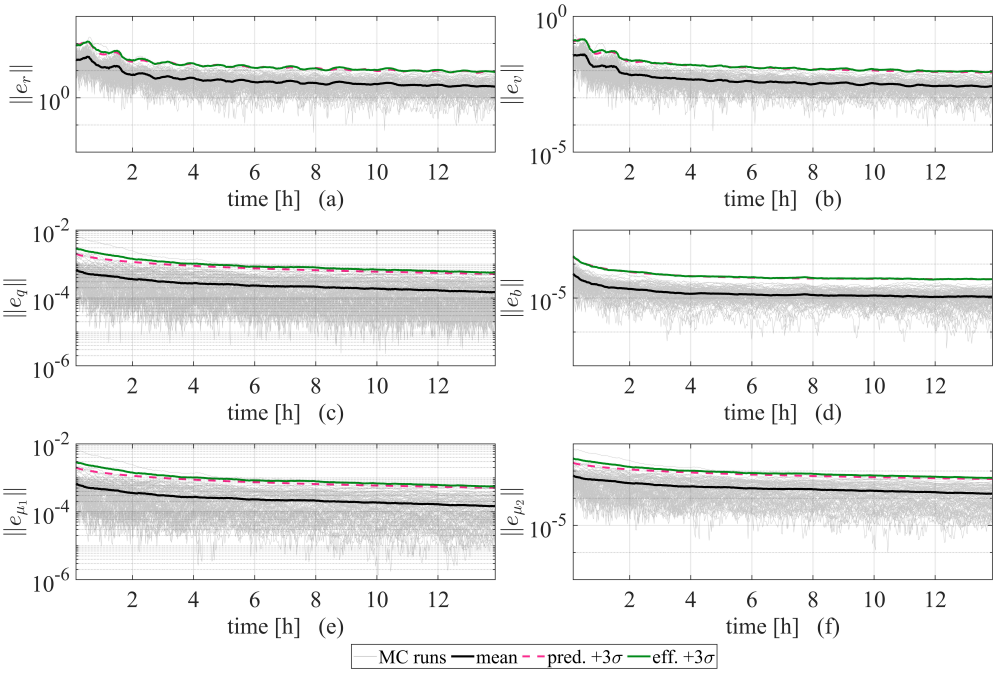


Fig. 14: State-group covariance diagnostic for the FM-UKF at $\Delta t = 90$ s.

Indeed, in the course step scenario, the FM-UKF and Level 3 FM-SGHQF reached the lowest final position error and attitude error, with NIS and ANEES near their exact expected values. The Level 2 FM-SGHQF kept its NIS near the expected level, but its final position error was nearly three times larger, and its ANEES stayed about two orders of magnitude above unity. A well-behaved innovation sequence was therefore not sufficient evidence of a consistent state covariance. The MEKF stayed bounded but was the least accurate, since it relies on mere linearization and cannot adequately account for distributions with heavy tails.

As expected, the Level 3 FM-SGHQF accuracy came at a high computational cost, while the FM-UKF showed a well-balanced trade-off among cost, consistency, accuracy, and robustness. The FM-UKF was the only estimator that met both the covariance-agreement and mean-timing criteria at both cycle intervals. Thus, its use is validated for the consequent hardware-in-the-loop testing with a dual-tracker configuration. There, measurement errors will come from processing real images rather than from the Gaussian noise model assumed here.

Statements and Declarations

Acknowledgments and Funding. The authors wish to acknowledge the support of this work through the National Aeronautics and Space Administration (NASA)

Established Program to Stimulate Competitive Research (EPSCoR) under grant number 80NSSC24M0110. An AI tool was used solely to assist with grammar editing and proofreading of the manuscript.

Competing Interests. The authors have no relevant financial or non-financial interests to disclose.

Data Availability. The data supporting the findings of this study were generated through numerical simulations as described in the manuscript and are available from the corresponding author upon reasonable request.

Clinical trial number. Not applicable.

References

[1] Christian, J.A.: Fundamentals of Spacecraft Optical Navigation. John Wiley & Sons, Ltd, Chichester, UK (2025). https://doi.org/10.1002/9781394267743

[2] Karimi, R.R., Mortari, D.: Interplanetary autonomous navigation using visible planets. Journal of Guidance, Control, and Dynamics **38**(6), 1151–1156 (2015) https://doi.org/10.2514/1.G000575

[3] Franzese, V., Topputo, F.: Optimal beacons selection for deep-space optical navigation. The Journal of the Astronautical Sciences **67**(4), 1775–1792 (2020) https://doi.org/10.1007/s40295-020-00242-z

[4] Andreis, E., Franzese, V., Topputo, F.: Onboard orbit determination for deep-space CubeSats. Journal of Guidance, Control, and Dynamics **45**(8), 1466–1480 (2022) https://doi.org/10.2514/1.G006294

[5] Andreis, E., Panicucci, P., Topputo, F.: Autonomous vision-based algorithm for interplanetary navigation. Journal of Guidance, Control, and Dynamics **47**(9), 1792–1807 (2024) https://doi.org/10.2514/1.G007926

[6] Krause, M., Thrasher, A., Soni, P., Smego, L., Isaac, R., Nolan, J., Pledger, M., Lightsey, E.G., Ready, W.J., Christian, J.A.: LONEStar: The lunar flashlight optical navigation experiment. The Journal of the Astronautical Sciences **71**, 33 (2024) https://doi.org/10.1007/s40295-024-00452-9 . Article 33

[7] Thrasher, A., Christian, J., Driessen, W., Inman, R., Pecourt, R., Lovelace, R., Marshall, M.: Development of the optical deep-space instrument for navigation (ODIN). In: 39th Annual Small Satellite Conference, Salt Lake City, Utah (2025). Paper SSC25-P2-40, NASA Technical Reports Server Document ID 20250005769

[8] Pittelkau, M.E.: Kalman filtering for spacecraft system alignment calibration. Journal of Guidance, Control, and Dynamics **24**(6), 1187–1195 (2001) https://doi.org/10.2514/2.4834

[9] Lai, K.-L., Crassidis, J.L., Harman, R.R.: In-space spacecraft alignment calibration using the unscented filter. In: AIAA Guidance, Navigation, and Control Conference and Exhibit, Austin, Texas (2003). https://doi.org/10.2514/6.2003-5563 . AIAA Paper 2003-5563

[10] Zanetti, R., D'Souza, C.N.: Observability analysis and filter design for the orion earth–moon attitude filter. Journal of Guidance, Control, and Dynamics **39**(2), 201–213 (2016) https://doi.org/10.2514/1.G001217

[11] Kikuchi, S., Shirai, K., Ishibashi, K., Wada, K., Yokota, Y., Honda, R., Kadono, T., Shimaki, Y., Sakatani, N., Ogawa, K., Sawada, H., Saiki, T., Mimasu, Y., Takei, Y., Sugita, S., Kouyama, T., Hirata, N., Nakazawa, S., Yoshikawa, M., Tanaka, S., Watanabe, S.-i., Tsuda, Y., Arakawa, M.: Simultaneous geometric calibration and orbit-attitude determination of Hayabusa2's deployable camera (DCAM3). Advances in Space Research **74**(2), 899–936 (2024) https://doi.org/10.1016/j.asr.2024.04.057

[12] Christian, J.A.: Optical navigation using planet's centroid and apparent diameter in image. Journal of Guidance, Control, and Dynamics **38**(2), 192–204 (2015) https://doi.org/10.2514/1.G000872

[13] Christian, J.A.: StarNAV: Autonomous optical navigation of a spacecraft by the relativistic perturbation of starlight. Sensors **19**(19), 4064 (2019) https://doi.org/10.3390/s19194064

[14] Franzese, V., Topputo, F.: Deep-space optical navigation exploiting multiple beacons. The Journal of the Astronautical Sciences **69**, 368–384 (2022) https://doi.org/10.1007/s40295-022-00303-5

[15] Lefferts, E.J., Markley, F.L., Shuster, M.D.: Kalman filtering for spacecraft attitude estimation. Journal of Guidance, Control, and Dynamics **5**(5), 417–429 (1982) https://doi.org/10.2514/3.56190

[16] Markley, F.L.: Attitude error representations for kalman filtering. Journal of Guidance, Control, and Dynamics **26**(2), 311–317 (2003) https://doi.org/10.2514/2.5048

[17] Markley, F.L.: Attitude estimation or quaternion estimation? The Journal of the Astronautical Sciences **52**(1–2), 221–238 (2004) https://doi.org/10.1007/BF03546430

[18] Crassidis, J.L., Markley, F.L., Cheng, Y.: Survey of nonlinear attitude estimation methods. Journal of Guidance, Control, and Dynamics **30**(1), 12–28 (2007) https://doi.org/10.2514/1.22452

[19] Markley, F.L., Crassidis, J.L.: Fundamentals of Spacecraft Attitude Determination and Control. Space Technology Library. Springer, New York, NY, USA

(2014). https://doi.org/10.1007/978-1-4939-0802-8

[20] Chang, L.: Multiplicative extended kalman filter ignoring initial conditions for attitude estimation using vector observations. The Journal of Navigation **76**(1), 62–76 (2023) https://doi.org/10.1017/S0373463322000443

[21] Zhu, H., Gui, H., Zhong, R.: Unscented schmidt-kalman filter on lie groups with application to spacecraft attitude estimation. Advances in Space Research **74**(11), 5713–5724 (2024) https://doi.org/10.1016/j.asr.2024.08.035

[22] Crassidis, J.L., Markley, F.L.: Unscented filtering for spacecraft attitude estimation. Journal of Guidance, Control, and Dynamics **26**(4), 536–542 (2003) https://doi.org/10.2514/2.5102

[23] Markley, F.L., Cheng, Y., Crassidis, J.L., Oshman, Y.: Averaging quaternions. Journal of Guidance, Control, and Dynamics **30**(4), 1193–1197 (2007) https://doi.org/10.2514/1.28949

[24] Zanetti, R.: A multiplicative residual approach to attitude kalman filtering with unit-vector measurements. The Journal of the Astronautical Sciences **57**(4), 793–801 (2009) https://doi.org/10.1007/BF03321530

[25] Zanetti, R., DeMars, K.J.: Fully multiplicative unscented kalman filter for attitude estimation. Journal of Guidance, Control, and Dynamics **41**(5), 1183–1189 (2018) https://doi.org/10.2514/1.G003221

[26] Julier, S.J., Uhlmann, J.K.: A new extension of the kalman filter to nonlinear systems. In: Kadar, I. (ed.) Signal Processing, Sensor Fusion, and Target Recognition VI, vol. 3068, pp. 182–193. SPIE, Bellingham, WA, USA (1997). https://doi.org/10.1117/12.280797

[27] Julier, S.J., Uhlmann, J.K., Durrant-Whyte, H.F.: A new method for the nonlinear transformation of means and covariances in filters and estimators. IEEE Transactions on Automatic Control **45**(3), 477–482 (2000) https://doi.org/10.1109/9.847726

[28] Julier, S.J.: The scaled unscented transformation. In: Proceedings of the 2002 American Control Conference, vol. 6, pp. 4555–4559 (2002). https://doi.org/10.1109/ACC.2002.1025369

[29] Julier, S.J., Uhlmann, J.K.: Unscented filtering and nonlinear estimation. Proceedings of the IEEE **92**(3), 401–422 (2004) https://doi.org/10.1109/JPROC.2003.823141

[30] Wan, E.A., Merwe, R.: The unscented kalman filter for nonlinear estimation. In: Proceedings of the IEEE 2000 Adaptive Systems for Signal Processing, Communications, and Control Symposium, pp. 153–158 (2000). https://doi.org/10.1109/

ASSPCC.2000.882463

[31] Kiani, M., Pourtakdoust, S.H.: Concurrent orbit and attitude estimation using minimum sigma point unscented kalman filter. Proceedings of the Institution of Mechanical Engineers, Part G: Journal of Aerospace Engineering **228**(6), 801–819 (2014) https://doi.org/10.1177/0954410013479072

[32] Challa, S., Bar-Shalom, Y., Krishnamurthy, V.: Nonlinear filtering via generalized edgeworth series and gauss–hermite quadrature. IEEE Transactions on Signal Processing **48**(6), 1816–1820 (2000) https://doi.org/10.1109/78.845944

[33] Smolyak, S.A.: Quadrature and interpolation formulas for tensor products of certain classes of functions. Soviet Mathematics Doklady **4**, 240–243 (1963)

[34] Barthelmann, V., Novak, E., Ritter, K.: High dimensional polynomial interpolation on sparse grids. Advances in Computational Mathematics **12**, 273–288 (2000) https://doi.org/10.1023/A:1018977404843

[35] Bungartz, H.-J., Griebel, M.: Sparse grids. Acta Numerica **13**, 147–269 (2004) https://doi.org/10.1017/S0962492904000182

[36] Jia, B., Xin, M., Cheng, Y.: Sparse gauss–hermite quadrature filter with application to spacecraft attitude estimation. Journal of Guidance, Control, and Dynamics **34**(2), 367–379 (2011) https://doi.org/10.2514/1.52016

[37] Jia, B., Xin, M., Cheng, Y.: Sparse Gauss-Hermite Quadrature Filter for Orbit Estimation. https://doi.org/10.2514/6.2010-7588 . https://arc.aiaa.org/doi/abs/10.2514/6.2010-7588

[38] Jia, B., Xin, M., Cheng, Y.: Sparse-grid quadrature nonlinear filtering. Automatica **48**(2), 327–341 (2012) https://doi.org/10.1016/j.automatica.2011.08.057

[39] Jia, B., Xin, M.: Vision-based spacecraft relative navigation using sparse-grid quadrature filter. IEEE Transactions on Control Systems Technology **21**(5), 1595–1606 (2013) https://doi.org/10.1109/TCST.2012.2214779

[40] Baek, K., Bang, H.: Adaptive sparse grid quadrature filter for spacecraft relative navigation. Acta Astronautica **87**, 96–106 (2013) https://doi.org/10.1016/j.actaastro.2013.02.002

[41] Ganganath, R., Servadio, S.: Fully Multiplicative Attitude and Orbit Determination for Deep space Navigation (2026). https://arxiv.org/abs/2607.10072

[42] Müller, A., Bischoff, M.: A consistent finite element formulation of the geometrically non-linear reissner-mindlin shell model. Archives of Computational Methods in Engineering **29**(5), 3387–3434 (2022) https://doi.org/10.1007/s11831-021-09702-7

[43] Mehra, R.K., Peschon, J.: An innovations approach to fault detection and diagnosis in dynamic systems. Automatica **7**(5), 637–640 (1971) https://doi.org/10.1016/0005-1098(71)90028-8

[44] Bar-Shalom, Y., Birmiwal, K.: Consistency and robustness of pdaf for target tracking in cluttered environments. Automatica **19**(4), 431–437 (1983) https://doi.org/10.1016/0005-1098(83)90059-6

[45] Ganganath, R., Servadio, S., Lee, D.: Star Tracker Misalignment Compensation in Deep Space Navigation Through Model-Based Estimation. arXiv preprint arXiv:2507.19838 (2025). https://doi.org/10.48550/arXiv.2507.19838 . https://arxiv.org/abs/2507.19838

[46] Ganganath, R., Servadio, S., Lee, D.D.: Compensating Star-Trackers Misalignments with Adaptive Multi-Model Estimation. arXiv preprint arXiv:2601.01130 (2026). https://doi.org/10.48550/arXiv.2601.01130 . https://arxiv.org/abs/2601.01130

Appendix A Calibrated Dual-Tracker Misalignment Prior

The residual optical-tracker misalignment prior is obtained from the dual-tracker MEKF–MMAE calibration developed in our previous work [45, 46]. Define the stacked misalignment vector as

$$\boldsymbol{\mu}_{12} = \begin{bmatrix} \boldsymbol{\mu}_1^\top & \boldsymbol{\mu}_2^\top \end{bmatrix}^\top \in \mathbb{R}^6. \tag{A1}$$

The calibrated prior mean used in the present study is

$$\bar{\boldsymbol{\mu}}_{12,0} = \begin{bmatrix} -4.633604 \\ 2.123688 \\ -5.863906 \\ -5.203131 \\ 2.082970 \\ -2.944855 \end{bmatrix} \times 10^{-3} \text{ rad}. \tag{A2}$$

The corresponding joint covariance is

$$P_{\mu,\text{prior}} = \begin{bmatrix} 8.454257571059261 \times 10^{-7} & 4.668092596057423 \times 10^{-9} & 2.987795351006544 \times 10^{-8} & 5.467574073314621 \times 10^{-9} & -2.623893120803446 \times 10^{-9} & 3.790756580497593 \times 10^{-8} \\ 4.668092596057423 \times 10^{-9} & 8.405045370489300 \times 10^{-7} & 1.802277097692081 \times 10^{-8} & 3.296511316971029 \times 10^{-9} & -1.580674355297684 \times 10^{-9} & 2.286693253942806 \times 10^{-8} \\ 2.987795351006544 \times 10^{-8} & 1.802277097692081 \times 10^{-8} & 9.530914229287266 \times 10^{-7} & 2.111523143706723 \times 10^{-8} & -1.013076221596536 \times 10^{-8} & 1.464150979870047 \times 10^{-7} \\ 5.467574073314621 \times 10^{-9} & 3.296511316971029 \times 10^{-9} & 2.111523143706723 \times 10^{-8} & 8.415563606206718 \times 10^{-7} & -1.851651104020295 \times 10^{-9} & 2.678761184709997 \times 10^{-8} \\ -2.623893120803446 \times 10^{-9} & -1.580674355297684 \times 10^{-9} & -1.013076221596536 \times 10^{-8} & -1.851651104020295 \times 10^{-9} & 8.385822108486143 \times 10^{-7} & -1.285513546593502 \times 10^{-8} \\ 3.790756580497593 \times 10^{-8} & 2.286693253942806 \times 10^{-8} & 1.464150979870047 \times 10^{-7} & 2.678761184709997 \times 10^{-8} & -1.285513546593502 \times 10^{-8} & 1.023450995570169 \times 10^{-6} \end{bmatrix} \text{ rad}^2. \tag{A3}$$

For each Monte Carlo realization, the true initial residual misalignment is drawn from

$$\boldsymbol{\mu}_{12,0}^{(m)} \sim \mathcal{N}\left(\bar{\boldsymbol{\mu}}_{12,0}, P_{\mu,\text{prior}}\right), \tag{A4}$$

while all estimators are initialized at the common prior mean,

$$\hat{\boldsymbol{\mu}}_{12,0} = \bar{\boldsymbol{\mu}}_{12,0}, \tag{A5}$$

with $P_{\mu,\text{prior}}$ used as the corresponding 6×6 block of the initial covariance. The cross-axis and cross-tracker covariance terms are retained. Numerical symmetrization and positive-definiteness regularization are applied only when required for covariance factorization.